ABSTRACT

HERRING, NICHOLAS FRANKLIN. Ray Effects Mitigation in S_N Problems through General Collision Monte Carlo Coupling and Numerical Validation of the THOR S_N Code for Nuclear Nonproliferation Applications. (Under the direction of Dr. Yousry Azmy).

Discrete ordinates (S_N) methods allow for computationally efficient solutions to radiation transport problems. However, S_N transport problems can suffer from a numerical phenomenon in their solution called ray effects. This problem occurs during the propagation of radiation in low in-group scattering regions far away from a localized source. Air is one low in-group scattering medium due to its small optical thickness. This unfortunately means that ray effects are common in nonproliferation applications since air regions are common in these problems. A proposed approach for mitigating ray effects is to simulate the first few collisions of a transport problem using a Monte Carlo method (which does not require any discretization but may be computationally expensive) and using the results of that simulation as a source for the S_N calculation. This "few-collided source" is expected to be distributed more uniformly in space and should lead to an S_N transport solution that exhibits less ray effects.

Through coupling the S_N code THOR (Tetrahedral High Order Radiation transport code) with the Monte Carlo code Hammer, promising results in the practical application of this method in systems which are not too highly scattering are obtained in this work. The method involves evaluating low collision-count scattered flux with Hammer while the higher scattered solution is calculated using THOR for a total flux solution obtained by combining the two results. Results show the coupling to be effective in removing visible ray effects from the solution of a test problem. Further analysis of the mitigation is performed on a simplified version of a real experimental model to establish that accurate detector responses can be computed using our new coupling method.

The development and testing of such a model is an integral part of this work as it will provide a benchmark problem for nonproliferation focused transport codes. Such a problem also serves as a numerical validation for the THOR code in nonproliferation detector-based applications. The specific model employed here is a simplified version of the full physical experiment configuration. This simplification is done so we can rely more on coarser cells, which allows for more computationally efficient calculations and allows us to resolve small features that can be difficult to accurately model using tetrahedral meshes.

The calculation resulted in a full model continuous energy MCNP result within 20% of the experimental count rates. Using the simplified model with multigroup cross sections gave results within 40% of the continuous energy count rate, indicating a large error introduced by our cross sections. Finally, the coupled Hammer and THOR results were less than 11% different from the multigroup MCNP calculations. These results were even better for a model not featuring the optional SNAP shield where they showed agreement to within 3% of the multigroup MCNP results. This result was an improvement from the accuracy obtained with the non-coupled THOR calculation which was only within 52% of the multigroup MCNP, indicating that ray effect mitigation through Monte Carlo coupling is effective.

Ray Effects Mitigation in S_N Problems through General Collision Monte Carlo Coupling and Numerical Validation of the THOR S_N Code for Nuclear Nonproliferation Applications

by
Nicholas Franklin Herring

A thesis submitted to the Graduate Faculty of
North Carolina State University
in partial fulfillment of the
requirements for the degree of
Master of Science

Nuclear Engineering

Raleigh, North Carolina

2018

APPROVED BY:

Dr. Yousry Y. Azmy Committee Chair	Dr. John Mattingly
Dr. Robert Hayes	

BIOGRAPHY

Nicholas Herring was born in Greensboro, North Carolina to James and Anita Herring. He was homeschooled by his parents all throughout middle school and high school. After high school, he attended North Carolina State University (NC State), where he obtained a BS in nuclear engineering. His education continued at NC State for graduate school in nuclear engineering. During the summers he has had the opportunity to work at Idaho National Lab.

ACKNOWLEDGMENTS

First and foremost, my thanks go to my advisor, Dr. Yousry Azmy. He has guided me through the thesis process and has been a major influence on the direction and style of my research for the work described here. In addition, I appreciate the willingness of Dr. John Mattingly and Dr. Robert Hayes to serve on my committee. I would particularly like to mention Dr. Mattingly's involvement in the experimental aspects of my thesis as he secured the ability for us to perform the experiments on the Beryllium-Reflected Plutonium (BeRP) Ball. Staff at Los Alamos National Laboratory and the Nevada National Security Site have proved invaluable in securing the permission and training required to preform our experiments as well as model info, in particular Jesson Hutchinson has provided much needed schematics and experimental information. Dr. Sebastian Schunert at Idaho National Laboratory and Raffi Yessayan at North Carolina State University have also provided invaluable assistance in understanding and effectively applying the THOR transport code that much of this work relies on. The work regarding the Monte Carlo code Hammer was performed by Dr. Brian Kiedrowski's team at the University of Michigan, so my appreciation extends to him and his team as well. I would also like to thank the Integrated University Program Graduate Fellowship for financially supporting my work as a graduate student and allowing me to pursue research topics of my interest. Finally, I would like to thank CNEC for providing this problem and for partially funding this work for the furthering of nonproliferation simulation and advanced modeling capabilities.

TABLE OF CONTENTS

LIST OF TABLES

LIST OF FIGURES

Chapter 1. Introduction

The problem of ray effects in transport calculations is important in nonproliferation and radiation shielding problems. Since the propagation of a localized source cannot be accurately calculated using discrete ordinates methods through low scattering media (such as air) ray effects are common in configurations involving detectors separated from a localized source by air. As such, efforts have been previously made to mitigate or eliminate ray effects in discrete ordinates transport calculations.

Perhaps the most common method of mitigation involves the tracing of rays from points used to approximate the localized source to computational cells where the flux is desired across the low scattering media. The radiation is then propagated and attenuated along these rays and an effective flux is rebuilt in the desired cells in order to compute a first collision source distributed in each cell. This method, sometimes referred to as the analytic point-kernel approach to cover its broader use in full transport solution codes, is used in several transport codes including the Denovo code that is part of the ADVANTG package [1]. Such an approach suffers from a few problems. Firstly, complex source geometries can require multi-point approximations which can be inaccurate or expensive to create. Additionally, the method can require prohibitively large numbers of rays for a complex/large region of importance to be traced to. The region of importance must be determined by the user ahead of time, and the source must be approximated automatically, or manually. Finally, such a method is semi-analytic in its approach to rebuilding the distributed flux from point values, with expressions that are often *ad hoc* (that is the methods are an engineering approximation and without explicit mathematically foundation).

Another approach is one that appears to be both intuitive and practical, and that is to increase the number of discrete angles in the angular quadrature of the S_N problem. Such a

method allows for ray effect mitigation with minimal additional effort on the part of the user preforming the calculations since the quadrature order is simply increased, assuming the high-order quadratures are available in the subject transport code. However, the traditional level symmetric angular quadrature sets have practical limitations on the order that they can be extended to. Special quadrature sets are often required for problems with severe ray effects, the making of which can be difficult. Additionally, even upon creation of such a quadrature set, the calculation with increased number of discrete angles becomes significantly more expensive, and the quadrature order that will significantly reduce the error from ray effects must be determined on a problem by problem basis.

An equivalent form of the discrete ordinates equation has been created using spherical harmonics equations to mitigate ray effects [2]. This method allows for a cheap calculation that mitigates ray effects. However as spherical harmonics equations contain the reciprocal of the total macroscopic cross section, this method can be unstable for regions with exceedingly thin optical thickness (such as air).

An analytic first collision source was also shown to be effective and applied in the first collision source codes GRTUNCL and GRTUNCL3D in two- and three-dimensional configurations, respectively, that are in use with the DOORS code collection among others [3]. This method involves the use of the analytic solution for a purely absorbing system to calculate uncollided flux at all distances from a distributed source. However, for complex sources and configurations this calculation can be prohibitively expensive.

The final method covered here for the mitigation of ray effects is through the coupling of Monte Carlo simulations to compute the first collision source. The previously cited Denovo code, in the SCALE code system, also makes use of such a method as an option for their first

collision source calculation [4]. Such a method begins by running a Monte Carlo simulation for uncollided flux. Once this flux is calculated throughout the system, it can be multiplied by scattering cross sections per computational cell to create a first collision source distribution throughout the domain to be used as the "external" source in a subsequent discrete ordinates calculation. Such a method benefits simultaneously from the lack of ray effects in Monte Carlo simulations of the uncollided flux, and the low computational costs of discrete ordinates methods for the rest of the solution. Such a calculation does assume that the flux field resulting from the source is dominated by uncollided particles on their way towards the region of importance (such as inside a detector). This assumption is generally good since ray effects are a phenomenon associated with materials with low collision rates.

It is a variation of this method that we adapt in our new mitigation strategy presented in this work. We propose a mitigation method that uses Monte Carlo techniques to simulate an arbitrary n–1 number of collisions and similarly uses the results from those collisions to compute an n^{th} collided source. This will enable the mitigation of ray effects to be more robust for systems where more than just the uncollided flux suffers heavily from ray effects.

The experiment used to verify our new method for mitigating ray effects and to validate the THOR code consists of the weapons grade plutonium BeRP Ball on a stand sitting on a table with detectors set up on the table. Previously, constructive solid geometry (CSG) models have been made for both the ball itself as well as for the detectors that we used (MC15 and SNAP) in a configuration suitable for modeling with MCNP.

The remainder of this thesis is organized as follows. In Chapter 2 we review previously related work. Here we introduce transport theory and methods of solving neutron transport problems. We additionally expand on our description and analysis of ray effects and the

established methods of mitigation. Finally, we examine previously performed experiments of the same style as the ones performed for this work.

In Chapter 3 we examine the experimental setup performed for this work. This chapter also investigates and draws conclusions from results measured in performing these experiments.

Chapter 4 introduces the MCNP models of the experiment that will serve as the basis of our computational systems. This chapter examines both the full MCNP model and its results created by Los Alamos, as well as the simplified MCNP model created for our computational experiments. The errors introduced by each change in the process of creating this model are quantified, recorded, and justified.

Chapter 5 discusses the development of the capabilities needed to perform our method of ray effect mitigation. First, the chapter introduces four capabilities to be introduced to THOR in order to enable easier problem computation and examination of results. This begins with discussing verification of the manner of introducing subcritical multiplication to THOR. Then a flux plotting method is discussed for use in visualizing computational results from THOR. This is followed by discussion of the mesh generation method for THOR compatible meshes. Finally, the method of converting SERPENT generated cross sections to THOR compatible data is introduced. The chapter then introduces and derives the general collision Monte Carlo to S_N coupling method to mitigate ray effects and describes the implementation of the method. Finally, the chapter introduces two different models to examine ray effects mitigation. The first features an isolated source in a cube of air for visual examination of ray effects. The second is a detector model described in Chapter 4 made in order to demonstrate the practical implications of ray effects.

Chapter 6 presents and discusses computational results using both pure S_N THOR calculations as well as coupled calculations. The results here demonstrate the effectiveness of the method in mitigating ray effects both visually and practically in nonproliferation applications.

Chapter 7 offers conclusions from results both experimental and computational in this thesis. The method and model are also discussed, and the chapter includes discussion of the numerical validation of this method and THOR for these types of problems. Finally, potential topics of further investigations are proposed and discussed.

Chapter 2. Review of Related Work

2.1 Neutron Transport Methods

2.1.1 Transport Theory and Equation

For systems where many neutral particles are interacting in a distributed physical space, time, and velocity, certain statistical rules may be better suited to describe the behavior of the system. The most common statistically-aggregated model used in neutron transport problems is the Boltzmann equation. Four postulates must be adopted to cast this equation [5]. First the particles being modeled must move freely most of the time and interact with each other only during collision events where collisions of more than two bodies are considered rare. Second, the average distance between collisions is much greater than the characteristic particle size. Third, the collision time must be much less than the time between collisions. Fourth, gradients of inhomogeneity in the system must be gradual for the particles being modeled compared to the scale on which they collide.

For neutron transport problems in shielding and reactor systems, these postulates hold in almost all circumstances. This leads to the applicability of the linearized Boltzmann equation in these applications. The specific form of the Boltzmann equation that is used in these problems can be derived through particle balance in a considered phase space. Such a balance derivation yields what is commonly known as the neutron transport equation,

$$\left[\frac{1}{v}\frac{\partial}{\partial t} + \vec{\Omega}\cdot\nabla + \Sigma_t(\vec{r},E)\right]\psi(\vec{r},E,\vec{\Omega}) = \int d\vec{\Omega}'\int dE'\,\Sigma(E'\to E;\vec{\Omega}'\to\vec{\Omega},\vec{r})\psi(\vec{r},E',\vec{\Omega}') + S(\vec{r},E,\vec{\Omega}) \quad (2.1)$$

where $\psi(\vec{r},E,\vec{\Omega},t)$ is the neutron flux distribution and magnitude at location $\vec{r}$, comprised of particles with energy E, moving along direction $\vec{\Omega}$, at time t. $\Sigma_t(\vec{r},E)$ is the total interaction

cross section and $\Sigma(E' \rightarrow E; \vec{\Omega}' \rightarrow \vec{\Omega}, \vec{r})$ is the cross section for particles with energy E' and angle $\vec{\Omega}'$ to produce particles of energy E and angle $\vec{\Omega}$. This integro-differential equation is a simplified form of the full Boltzmann equation and is useful and suitable for work in neutron transport.

But this equation is complicated in nature and it provides analytic solutions in only a few select cases that are generally highly simplified and not sufficient descriptors for the real-world applications. This fact prompts numerical methods for obtaining approximate solutions in low- to high-fidelity models of realistic applications. Methods for direct numerical solutions of this equation often require discretization of the neutron energy spectrum [6]. Such discretization is rooted in the fundamental concept that conservation of reaction rates in the system is essential for a useful solution to the transport equations. This concept stems from the fact that the behavior of a neutron system and most quantities of interest to nuclear scientists and engineers is driven by neutron interactions with the host medium. From neutron streaming across regions, to reactor power levels and associated local peaks of production through fission, to the interaction rate in a detector providing a response, the conservation of reaction rates is essential to a useful solution to the transport equation. As such the defined multigroup, or energy discretized, cross sections optimally take such a form as to conserve corresponding reaction rates in Eq. 2.2 throughout all regions of the domain,

$$\Sigma_{\mathrm{x,g}} = \frac{\int_{E_g}^{E_{g-1}} dE\ \Sigma_x(E)\phi(E)}{\int_{E_g}^{E_{g-1}} dE\ \psi(E)} \qquad 2.2$$

where $\Sigma_x(E)$ is the cross section associated with interactions of type x. Definitions similar to Eq. 2.2 yield the multigroup form of the transport equation,

$$\left[\frac{1}{v_g}\frac{\partial}{\partial t} + \vec{\Omega}\cdot\nabla + \Sigma_{t_g}(\vec{r})\right]\psi_g(\vec{r},\vec{\Omega},t)$$
$$= \int d\vec{\Omega}' \sum_{g'=1}^{N_g} \Sigma_{g'\to g}(\vec{\Omega}'\to\vec{\Omega},\vec{r})\psi_{g'}(\vec{r},\vec{\Omega}',t) + S_g(\vec{r},\vec{\Omega},t) \quad (2.3)$$

where $\Sigma_{t_g}(\vec{r})$ is the total cross section effective in group g and $\Sigma_{s_{g'\to g}}(\vec{\Omega}'\to\vec{\Omega},\vec{r})$ is the production cross section in group g from incident neutrons in group g'. Many practical problems in neutron transport are considered as steady state problems, causing the time derivative term to vanish. For the remainder of this work, discussion of neutron transport will be considered exclusively for steady state problems unless otherwise noted.

For complicated geometries there are a few methods of dealing with the angular dependence of the neutron flux. One method is the discrete ordinates method, which solves the solution along discrete rays that then influence other rays in the set via coupling in the production term. This method will be expanded on later in the discussion.

Another common method of angular discretization is the expansion of the scattering cross sections through Legendre polynomials and expansion of the flux in Spherical Harmonics. Limiting the set of polynomials by truncating an angular derivative yields the spherical harmonics equations, or the P_N approximations [7]. This is often performed by truncating the spherical harmonics equations at N=1 to give the P_1 equations leading to Fick's law. This in turn gives the so-called neutron diffusion equation. This equation is commonly used in reactor calculations as it is generally much cheaper and simpler to solve compared to the full transport equation. However, no angular information is retained in diffusion theory for the flux, and this can result in low accuracy in regions of highly anisotropic flux.

The boundary conditions for the transport equation can be generally expressed as

$$\psi(\vec{r} \in \partial V, E, \vec{\Omega}, t) = \Gamma(E, \vec{\Omega}, t) \text{ for } \hat{n} \cdot \vec{\Omega} < 0 \quad (2.4)$$

where $\hat{n}$ is the outward normal vector of the bounding surface ∂V at the point r. These conditions can take a variety of forms including reflective boundary conditions, vacuum boundary conditions, and incident flux boundary conditions.

2.1.2 Monte Carlo Simulations

Solutions of the neutron transport equation can be obtained without solving the transport equation. Perhaps the most common method involves direct simulation of particle histories through Monte Carlo methods of sampling collision events based on the underlying neutron physics [8].

The standard application of this technique involves randomly starting a simulation of a particle history somewhere in the domain based upon a defined probabilistic physical distribution of the source in the domain. For example, if the source is defined to be evenly distributed over a sphere's volume, the particle will be sampled somewhere in the sphere with all locations in the sphere bearing an equal probability of being sampled. The particle is then sent in a random starting direction based on the definition of the angular distribution of the source (often isotropic for an external source).

The particle's trajectory is traced along this starting direction with probability of interaction in each region it moves through based upon the total cross section of the medium in that region, which in turn gives the region a defined optical density. This optical density gives the particle a chance to interact in a region or to move through an entire region without interaction along its current trajectory, based upon pseudo-random number sampling. If the particle is determined not to interact, it continues its current direction until either interacting in another region or exiting the defined problem domain. If the particle is determined to interact,

the interaction occurs somewhere along the path in the region determined by a random sampling based on the optical thickness. The type of interaction that occurs is also determined by a random sampling based on the relative magnitude of the cross sections for different interaction types. If the interaction produces new neutrons, through fission or scattering, the secondary neutrons are now given a random direction from that point based on the angular distribution of the neutron production (usually isotropic for fission but often anisotropic for scattering).

For an external source problem, all sampled particles are followed until they have been eliminated fully by either exiting the domain or interacting in a manner that does not produce secondary neutrons (absorption into a nucleus). This is done many times and the overall results are interpreted to effectively give a solution to the neutron transport equation in the system with related statistical error based on the number of particles started. Clearly this approach cannot be expected to accurately predict the behavior of a single neutron as the probabilities do not represent individual event physics. However, for many-particle simulations (as is required for the Boltzmann equation to be valid), the behavior of the system can be well modeled by Monte Carlo techniques.

Monte Carlo techniques have a few beneficial characteristics that methods for directly solving neutron transport equation generally lack. First, they can utilize more accurate geometries and do not require decomposition of physical geometry into cells. Objects are usually defined using constructive solid geometry (CSG) which allows exact and human readable expression of a geometry composed of combinations of geometric concepts, such as spheres, cylinders, and planes. Additionally, Monte Carlo simulations depend on full probabilistic distributions for neutron interactions, and therefore do not suffer the common deterministic difficulty of relying on multigroup cross section collapsing. This allows a Monte Carlo solution

to provide a more complete model of the neutron flux energy spectrum compared to a deterministic method. It is for this reason that a common method of multigroup cross section generation involves the use of Monte Carlo solutions of simplified problems to produce spectra at various energy cutoffs to preserve reaction rates in accordance with Eq. 2.2. These cross sections from simplified problems can then be used in more complex, but similar, systems for the faster deterministic methods to solve.

The biggest problem afflicting Monte Carlo techniques is the cost associated with the simulation process. Because the uncertainty in the computed results is inversely proportional to the number of particles sampled, complicated systems may require a prohibitively large number of simulations to generate an adequately accurate result. There are a few ways to mitigate this cost though. Firstly, since neutron systems are generally modeled for static environments, the cross sections of regions are unchanging in the model regardless of neutron interactions. For this reason, each particle can be treated independently without respect to other particles in the system. Such independence opens many possibilities in the realm of parallel computations for Monte Carlo simulations. Secondly, variance reduction techniques exist to reduce the uncertainty in the simulation results without incurring a significant increase in the computational cost. These techniques range from intuitive tactics such as factoring in path length in a regions flux tally, to more complex concepts such as statistical weight reduction of particles instead of killing them with absorption or system leakage.

2.1.3 Hammer

The Hammer code is one such Monte Carlo transport solver [9]. The Hammer code was developed with the intention of supporting deterministic methods for solving neutron transport problems, specifically to reduce ray effects in regions dominated by low scattered flux. The

Hammer code is different from many common Monte Carlo solvers in that it does currently rely on multigroup cross section information. This improves the speed of the calculations, and the ease with which the results may support deterministic codes, however it does mean that the errors incurred by multigroup cross sections are present in Hammer results.

Hammer's system geometry is based off of the standard method of CSG in 3D, however it supports flux tallying on tetrahedral cells after the simulation has completed. The tallying is done by mapping interaction collision points to the cells in which they occur. This tally is finally compared to the number of particles started and divided by the total cross section of the cells to determine a flux in the cell. This tallying allows for easy input into deterministic codes that break up the problem domain into tetrahedral cells. Hammer also supports a number of variance reduction techniques to improve the quality of flux estimation in regions of low interaction rate.

Perhaps the most important feature of Hammer's capabilities for supporting deterministic codes is the option to kill off particles after a certain number of collisions, and scoring all interactions based on their collision count. Such tracking of collision count allows for an accurate output of n^{th} collided neutron flux throughout the problem domain. The method in which deterministic codes can be supported by Hammer requires flux of n^{th} collided neutrons as well as all flux from lower collision-count neutrons. That is to say, the sum of all flux from uncollided flux to n^{th} collided flux. This is necessary to create a full description of the flux solution, as will be explained later, and this feature is supported in Hammer.

2.1.4 Discrete Ordinates

For deterministic methods of solving the transport equation the angular domain must be discretized in order to permit numerical solution. One of the most common methods of achieving this purpose involves the use of the discrete ordinates approximation. At its foundation, the

method consists of solving the transport equation along a set of discrete angular directions [10]. In three-dimensional Cartesian geometry the discrete ordinates, or S_N equations, are formulated as Eq. 2.5 with the effective distributed source described by Eq. 2.6. These equations represent the case of steady state multigroup neutron transport where all the secondary particles are emitted isotropically,

$$\left[\mu_n \frac{\partial}{\partial x} + \eta_n \frac{\partial}{\partial y} + \xi_n \frac{\partial}{\partial z} + \Sigma_{t_g}(\vec{r})\right] \psi_g(\vec{r}, \vec{\Omega}_n) = Q_g(\vec{r}) \tag{2.5}$$

$$Q_g(\vec{r}) = \frac{1}{8} \sum_{g'=1}^{N_g} \Sigma_{g' \to g}(\vec{r}) \sum_{n=1}^{N(N+2)} w_n \psi_{g'}(\vec{r}, \vec{\Omega}_n) + S_g(\vec{r}) \tag{2.6}$$

Here the discrete ordinates quadrature set is made up of unit vectors $\vec{\Omega}_n = \mu_n \hat{\imath} + \eta_n \hat{\jmath} + \xi_n \hat{k}$ so that $\mu_n^2 + \eta_n^2 + \xi_n^2 = 1$. The quadrature set also includes direction weights w_n to allow for accurate integration over the unit sphere using the quadrature set as indicated in the secondary particles production term in Eq. 2.6. Level symmetric sets have historically been very common in their use in discrete ordinates codes and many codes today have them as one of the common options. As such much of the discussion here will focus on level symmetric sets. Such sets provide N(N+2)/8 ordinates per octant and similarly N(N+2) directions across the entire unit sphere by reflecting the discrete ordinates from the first octant into the other seven octants.

These quadrature sets generally have practical restrictions though. One of the most common sets is the LQ_n set associated with the Legendre Polynomials. This set is useful in producing level symmetric quadratures up to S_{20}, however at S_{22} negative weights begin to appear. As such the highest order set of this type used is generally the S_{16} set, however even this set is rarely utilized as the large number of angles incurs a large and often prohibitive computational cost.

In external source application, the discrete ordinates equations are iteratively solved using a zero-flux initial guess. Such an initial guess means that each subsequent iterate of the discrete ordinates equations can be interpreted as the flux of particles that have experienced up to one more collision than the previous iteration, with the first iterate interpreted as the uncollided flux.

The physical interpretation of solving the discrete ordinates equations in this manner is computing the uncollided flux with the transport equation solely from particles emitted by the external source then traveling along the discrete ordinates in the spatial domain. The secondary production from this flux is then calculated in each cell using the cell's effective secondary production cross section. This leads to secondary production in the cell along all discrete directions based on the angular distribution of the production. This leads to regions in which the secondary production is high to tend to have secondary sources that are better distributed along directions in that region compared to regions where the secondary production is low.

If the flux is dominated by neutrons that have experienced only a few scattering events emitted from a localized source, then there exists a risk that the flux will not be well distributed along all directions in regions far from the localized source. This risk comes from the fact that only directions that trace back directly to the source will see the uncollided flux. As such, if the uncollided flux is dominant, the secondary production will in turn be low, resulting in flux focused along the rays that "see" the source. This results in the numerical artifacts known as ray effects and can be one of the biggest errors incurred in a discrete ordinates calculation. These artifacts prompt much of the work presented in this thesis and will be discussed at length later.

Discrete ordinates methods tend to be some of the fastest and most efficient methods for solving neutron transport problems. They retain angular flux information, unlike the diffusion equation, and they support angular dependence of the scattering cross sections usually via

projections onto Legendre Polynomials. As the angular fluxes along different angles are mutually independent in each sweep assuming Cartesian geometry and explicit boundary conditions, the potential for high degrees of parallel processing exists. There are also several iterative acceleration techniques that can be applied to solving the transport equation with the discrete ordinates approximation. Many of these are dependent on efficiently solving some form or variation on the spherical harmonics equations to estimate what the final flux should look like. All this leads to discrete ordinates methods often being seen as a good middle ground in terms of computational efficiency, easily beating the speed of continuous energy Monte Carlo but often slower than diffusion solutions, and solution accuracy, better describing angular flux effects than diffusion but maintaining errors of energy, space, and angle discretization's that are not incurred in Monte Carlo simulations. Instead, the latter incurs quantifiable statistical errors.

2.1.5 THOR

The THOR (Tetrahedral High-Order Radiation) transport code is a steady-state, multigroup, discrete ordinates transport solver for 3D, unstructured tetrahedral meshes [11]. THOR is currently maintained by the Consortium for Nonproliferation Enabling Capabilities (CNEC) and draws its origin from Dr. Rodolfo Ferrer's dissertation at Pennsylvania State University [12]. THOR solves the discrete ordinates equations on tetrahedral cells using the method of short characteristics where spatial moments of the flux are solved along characteristics traversing a cell, thus providing boundary conditions for the cell to interface with the flux in neighboring cells. The within-cell angular flux moments also enable evaluation of angular moments that facilitate the computation of the distributed source of secondary particles in an iterative manner as described above.

THOR supports eigenvalue solutions for supercritical, subcritical, and critical systems as well as external source solutions for non-multiplying and subcritical systems. THOR supports both isotropic and anisotropic scattering and has a variety of built-in angular quadrature sets. Recent applications of THOR include nonproliferation scenarios to solve complicated three-dimensional configurations involving source detection, shielding, and criticality.

As a discrete ordinates code, THOR suffers from errors introduced by energy and angular discretization. Additionally, spatial errors are present due to using cell moments of the flux to determine secondary production density-rates as well as the inability of tetrahedrons to fully describe curved geometries. But, with good cross sections and a well resolved unstructured mesh, these errors are often acceptable. A bigger concern for THOR in shielding and nonproliferation applications is ray effects.

As a transport code, THOR is an effective application of high order discrete ordinates equations and can provide fast three-dimensional solutions with highly efficient parallel capabilities. As such its use in three-dimensional nonproliferation applications remains of great interest to CNEC. This then prompts efforts to mitigate ray effects for the THOR code to enable more accurate and realistic neutron transport solutions in those applications.

2.2 Ray Effects

2.2.1 Description of Effects

Discrete ordinates methods solve the radiation transport equation along discrete angles in phase space. If the in-group scattering term is sufficiently large, the source due to collisions of the transported particles, or secondary source, is well distributed throughout the problem geometry. However, in low in-group scattering media the secondary source does not illuminate large patches of the problem domain far removed from a localized source. This results in solution

propagation only along angles that directly trace back to the localized source. Such “ray effects” can result in non-physical flux profiles that exhibit low illumination of cells not along the rays that reach back to the source, as well as over estimation of the flux along the rays.

Anomalous calculation results were first observed in 1965 from discrete ordinates approximations to the two-dimensional Boltzmann transport equation [13]. At about the same time similar inconsistencies in 2-D S_N calculations were noticed. It was gradually realized that the anomalies were not numerical truncations errors but due to the discrete ordinates formulation. With a limited number of discrete angles, there are a limited number of directions along which streaming can occur. So, neutron flux contributions in a region far from a localized source are limited to locations where angular directions in the quadrature set can be traced back directly to the localized source.

Though 2-D S_N computations have been practiced since 1959, these “ray effects” were not recognized in discrete ordinates until 1965 and it was theorized that this may be because the discrete ordinates formalism was derived by heuristic arguments for finite phase space cells [13]. The nature of these ray effects in the discrete ordinates approximations have been examined. It was pointed out that the severity of the ray effects is dependent upon the nature of the sources. Highly localized sources provide harsher ray effects as they result in more "dead zones" with respect to streaming characteristics. An example is shown in Fig 2.1 copied from [13], where the medium is a pure absorber, so the source is only present in the rectangular area on the right side of the diagram.

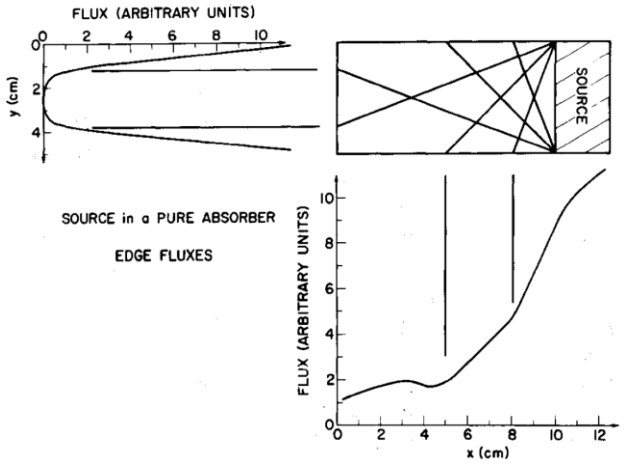

Figure 2.1: Monoenergetic Ray Effects in Discrete Ordinates Solution.

The problem shown featured a highly localized source. The characteristic directions from the source corners are shown in the figure, resulting in a dead zone on the far-left boundary where none of the characteristic curves both intersect the source on the far right, and the observation point on the far left. This results in all characteristic curves streaming into this triangular dead zone to be streaming zero source from a discrete ordinates perspective. This is clearly seen to be wrong as in the real world the dead zone points would experience a flux that is not only similar, but assuming the source is uniformly distributed in its region, but even larger than at the corners, which are seen to experience a positive flux. It should be noted here that ray effects are a geometric phenomenon therefore energy discretization is irrelevant to the demonstration of these effects.

A more complex case that was examined in [13] was the situation of four local fuel elements present in an absorbing material. An unexpected case of higher top flux than bottom flux was observed in the S_2 calculation, which was then mitigated by the higher order S_4 calculations. However, both showed an unexpected peak in the absorbing channel. It was conjectured that this may be due to lower absorbing properties of the channel. But it was discovered in the full results that this peak is actually caused by a confluence of flux ridges from

the four different sources along the 45^o angle, which is present in all S_N orders and angular sets. This local maximum at the channels was determined to be a subtler ray effect than that on the boundary but present for all orders of discrete ordinates equations.

The potential problems with ray effects in shielding and detector problems for S_N methods is immediately apparent. For a detector a distance away from a localized source, the rays may cause one of two issues. The first potential issue is that no rays may intersect both the local source and the local detector. The primary rays along the source missing the detector in this way would result in a count rate far below the physical expectation if the region between the source and the detector is composed of a low scattering material. This is because practically no particles will be transported from the source to the detector in this calculation.

Alternatively, the opposite, yet no less concerning, error is also possible. Since the discrete ordinates equations have no explicit term for geometric attenuation, the flux along the rays that intersect the source is subject to only material attenuation when compared to the source strength. Since ray effects are most common in low interacting regions, and low scattering regions tend to also have low total interaction rates, the flux along the ray ends up being significantly large compared to the physically expected value. Such large flux rays intersecting with a detector could result in significantly higher count rates in the detector than physically expected.

In the end, the best-case scenario for a problem with ray effects would be the cancellation of errors. Having offsetting number of peaks and troughs of interaction from the source along the rays going through low scattering regions. However, such a case is made increasingly unlikely as the region affected by ray effects becomes larger and the detector goes further from the localized source.

It therefore becomes clear that nonproliferation and shielding problems are perhaps the most affected by ray effects. Most such problems have large regions of air separating a very localized radiation source from a target model or point detector. Propagation through air with discrete ordinates equations results in massive ray effects as the secondary source production diminishes due to low optical thickness of air. As a result, dose or detector count rate estimates are often inaccurate when computed using just discrete ordinates methods, unless one is lucky enough that a cancellation of errors occurs.

However, the impact of ray effects reaches beyond just nonproliferation and shielding problems. While it is often assumed that ray effects are small or negligible in a large-scale reactor, due to fission sources that are often well distributed and the presence of highly scattering materials, studies have shown that ray effects can be a significant issue in fast reactor simulations [14]. Indeed, design studies of fast reactors with local heterogeneities, such as non-fuel control rods or instrument channels, have shown that power distributions in such designs are badly distorted when computed by low-order discrete ordinates quadratures. This error appears to be severe enough to raise concerns that thermal-hydraulic calculations using results from such equations may result in improper distribution of coolant flow and local overheating. So, while this work may primarily concern itself with ray effects and their mitigation for the purpose of nonproliferation applications, it should be kept in mind that ray effects, and by extension the need for their mitigation, appear in a variety of nuclear applications.

2.2.2 Mitigation Through Special Quadrature Sets

The most direct method of ray effect mitigation is through increasing the number of angles comprising the S_N quadrature set employed in the calculation. While ray effects must still be present for any finite number of angles, the chance that a sufficient number of peaks and

troughs will intersect a given location of interest, such as a detector, is drastically increased by having the location closer to the source, and by increasing the number of discrete directions to solve along. Such increase in spatial directions has been investigated [15]. Results showed that S_2 calculations provide a substantially less accurate solution in cases where severe ray effects are observed compared to S_{16}. However, it was illustrated that even with this remedy there are still ray effects contaminating the solution and they can exhibit defects requiring even higher order angular quadratures, which is not a practical remedy in terms of computational costs. A problem with a square source centrally located source in a square domain with $c = \frac{\Sigma_s}{\Sigma_t} = 2/3$ was solved in [15] and yielded results that demonstrated severe ray effects. Even with a S_{16} (144 directions) solution the ray effects are still quite visible, and this in a problem where the source covers an entire quarter of the domain and the scattering is nonzero. The fact that 144 directions is not sufficient to eliminate the distortion of the flux at the domain's edge suggests that simply increasing the number of discrete ordinates is unlikely to be yield a satisfactory solution to the problem of ray effects in a general setting. This is especially true in detector problems where sources tend to be physically small in comparison to the entire domain size.

Alternatively, special quadrature sets have been proposed and examined [15]. These quadrature sets are usually specific to a given problem, not generally applicable. One example involves arranging directions to preserve rotational invariance properties of the divergence operator. Results of numerical tests for the same square-in-square configuration described above using these sets (called R_N sets) were examined in [15].The distortions are reduced better than with the standard level symmetric quadrature sets originally used to show ray effects, however even with the expensive R_{16} set, visible ray effects persisted. The examined specialized sets proved to be more effective than the standard sets in reducing ray effects, however the

improvement is not significantly sufficient to avoid extremely high-order sets in more extreme cases.

In any case, it seems unlikely that special quadrature sets can provide a sufficient and general solution to ray effects that afflict discrete ordinates methods. Additionally, while increasing the order of the discrete ordinates quadrature set does show reduction in ray effects in general, such a method may require prohibitively large number of angles to solve problems of large physical extent suffering from severe ray effects.

2.2.3 Mitigation Through Spherical Harmonics Equivalence

Not relying on a collocation approach to angular discretization, the projection-based spherical harmonics method is immune to ray effects. This property has motivated the creation of discrete ordinates equations that are equivalent to the spherical harmonics equations. This method was implemented for the abovementioned square-in-square test problem [13]. The flux profile associated with the modified S_2 equations suffered from no ray effects, while the standard S_2 solution had clearly visible ray effects. The flux profile for the spherical harmonics equivalent solution matched exactly with a spherical harmonics solution of the problem.

A variation on this approach uses an interpolation method to formulate a proper fictitious source and boundary conditions for the problem to make it equivalent to the spherical harmonics [2]. This method results in a consistently high order method in the transformation between the discrete ordinates equations and the spherical harmonics equations, i.e. $S_N \rightarrow P_N$ equivalency. In fact, a general method of transformation to make any S_N set of equations equivalent to P_N equations has been demonstrated [2]. Such a method shows that for any discrete ordinates order, this method is possible.

The fictitious source method has been one of the most studied methods for spherical harmonics equivalence [16]. These sources seek not to attempt an entire transformation of the discrete ordinates equations to achieve equivalence with the spherical harmonics equations, rather they introduce a derived fictitious source term that will enforce the equivalency. The goal of such methods is to create situations were standard methods of solving the discrete ordinates equations can still be utilized but with the added source term to give spherical harmonics qualities to the solution. However, it must be recognized that derivation of the spherical harmonics equivalent source is non-trivial and unique for each quadrature order of discrete ordinates equations. Composing the source involves expanding the scattering cross section, angular flux, and external source using spherical harmonics, then inserting these newly expanded terms to the transport equation and applying the recursion formulas for the spherical harmonics. Comparison between this resulting equation and the S_N equations yields a fictitious source to give equivalence.

While this method does seem promising for application in trouble regions to eliminate ray effects, there is a concern arising from its equivalence to the spherical harmonics equations that normally include the reciprocal of the host material total cross sections. This division may be acceptable to resolve ray effects in highly absorbing media where the total cross section is reasonably large but the scattering ratio is small. However, for configurations common in detector and nonproliferation applications, which often include air, both total and scattering cross sections are very small so that division by the former may cause instability in the solution. Such an issue prompts the search for alternative methods of ray effect mitigation.

2.2.4 Mitigation Through Semi-Analytic Method

Mitigation of ray effects is possible through a more analytic approach. The GRTUNCL code was created for use with the two-dimensional transport code DORT and showed practical application of an analytic method for mitigating ray effects [17]. GRTUNCL solves for an uncollided flux throughout the domain analytically and is then transformed through *ad hoc* methods to create cell averaged scalar flux, which then in turn provides a first collision source to the DORT code. The computational method employed for this approach begins with

$$\phi_{u,g}(\vec{r}_i) = \sum_k S_g(\vec{r}_k) e^{-\beta_g(\vec{r}_k,\vec{r}_i)} \frac{\Delta A_k}{4\pi|\vec{r}_i - \vec{r}_k|^2} \qquad 2.7$$

Here $\phi_{u,g}(r_i)$ is the uncollided scalar flux in energy group g at location $\vec{r}_i$ due to an isotropic distributed source spanned by the discretized points $\vec{r}_k$. $S_g(\vec{r}_k)$ is the number of source particles emitted per unit time at point $\vec{r}_k$ across the area associated with that source disk ΔA_k. $\beta_g(\vec{r}_k,\vec{r}_i)$ is the number of mean free paths along the vector from $\vec{r}_i$ to $\vec{r}_k$. Evaluating this equation gives an estimate of the uncollided scalar flux at point $\vec{r}_i$, where the primary error incurred is the approximation of a distributed source by a set of point sources. The result is then plugged calculated for Eq 2.8 to provide a first collision source for the computational cell centered at r_i

$$S_g(\vec{r}_i,\vec{\Omega}) = \sum_l \sum_m \frac{A^{l,m}(\vec{\Omega})}{4\pi} \sum_{g'} \Sigma^l_{g'\to g}(\vec{r}_i) \sum_k S_g(\vec{r}_k) e^{-\beta_g(\vec{r}_k,\vec{r}_i)} \frac{A^{l,m}(\vec{\Omega}_k)\Delta A_k}{4\pi|\vec{r}_i - \vec{r}_k|^2} \qquad 2.8$$

This is now a space, angle, and energy dependent first collision source derived from Eq. 2.7 representing the uncollided flux. Here $\vec{\Omega}_k$ represents the unit vector from $\vec{r}_i$ to $\vec{r}_k$, $A^{l,m}(\vec{\Omega})$ are the reduced surface harmonics resulting from 2D symmetry, and $\Sigma^l_{g'\to g}(\vec{r}_i)$ are the lth coefficients

in the Legendre expansions of energy group-to-group scattering cross sections. All this together provides an analytic estimate of first collision source from a set of point sources.

The procedure of implementation goes as follows. First the geometry is described with the same spatial mesh used for the DORT problem. Next the uncollided flux is calculated for each selected spatial point and energy group. Then the first collision source is calculated for each point, energy and angular moment and written to an output file. Finally, the first collision source is used as DORT input in the form of an anisotropic fixed source array. DORT can then calculate the fully collided flux angular moments and combine them with the uncollided flux moments produced by GRTUNCL to get the total flux in the system.

This method was implemented and developed specifically for two-dimensional r-z geometry to go along with the transport code DORT, however there is no reason such a method could not be applicable in any geometric system. In fact, the method has been expanded to full 3D application in x-y-z geometry [18] and later r-θ-z geometry to compute first collision source moments [19]. Specifically, the r-θ-z application was used to mitigate ray effects in the TORT three-dimensional discrete ordinates computer code. The method was applied to the problem geometry composed of a cylinder of air containing a semicircular wall shielding a source.

This problem involved a gamma ray point source in the center of a semicircle concrete shield. The height of the source was 20m from the surface of the ground, or halfway up the 40m shield. The results of the calculation without GRTUNCL3D first collision source showed severe ray effects for the pure TORT calculation. Then combination with GRTUNCL3D demonstrated major mitigation of the ray effects in the air. The use of GRTUNCL3D was also demonstrated in [20] employing a complex geometry and computing dose rate. The calculations succeeded in

eliminating most primary ray effects using GRTUNCL3D and demonstrated the practical application of the method.

This method is not without limitations though as its computational cost becomes prohibitive for general problems. For an arbitrary source distribution discretized into a set of point sources, r_k, the contribution from each point source must be computed thus conferring a computational cost that is directly proportional to the number of point sources, per Eq 2.8. Additionally, complex geometries and fine meshes may require many field points, r_i, for first collision sources to be calculated at. This all can mean that for complicated meshes and source distributions, the costs associated with implementing a semi-analytic solution can be prohibitive.

This method is generally effective and efficient in simple geometries with simple source distributions. However even in such situations the method is still limited by its inability to estimate sources of higher collision orders than first. As such, in problems where severe ray effects are prominent in higher collided flux and higher collided particles dominate the flux distribution, one can expect little mitigation through application of the analytic first collision source method.

2.2.5 Mitigation Through Point-Kernel Method

The point-kernel method for radiation transport is a simplified method for considering a point source propagation through a medium [21]. As shown in Fig 2.2, the flux is attenuated along the rays drawn from the point source with attenuation dependent upon distances traveled through media to the target.

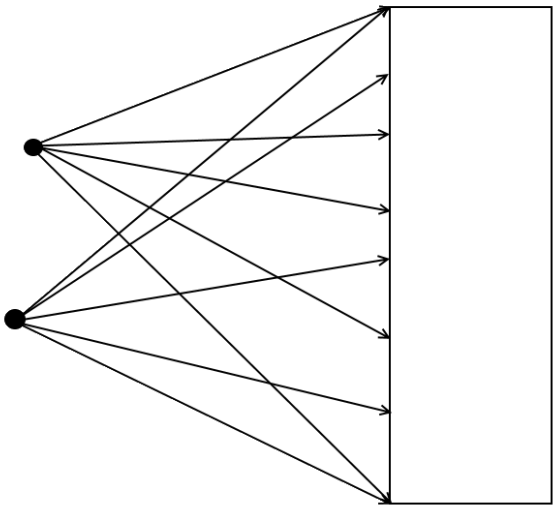

Figure 2.2: Point-Kernel Method.

The rebuilding of the flux is then done for the target cells that the ray is traced to. Such rebuilding is *ad hoc* with methods that are dependent upon cell shapes, location in the cell the lines are drawn to, and cell optical thicknesses.

For a problem using the point-kernel method to mitigate ray effects, the most common method is to ignore scattered radiation buildup, a reasonable assumption in our target applications since the problem area likely has a very low scattering rate. This now makes the calculated flux the uncollided flux, able to become the first collision source in a like manner to the analytic method. Once the uncollided flux is traced and attenuated to the cells it must be rebuilt into cell averaged scalar flux. The rebuilt flux is then multiplied by the scattering cross sections to create a first collision source, which is used to solve the rest of the problem using discrete ordinates method [22].

Such a method may require tracing many rays in order to achieve acceptable accuracy. The total number of rays is equal to the number of cells to be traced to multiplied by the number of discretized point sources multiplied by the number of rays needed for each cell. This results in cases requiring prohibitively large numbers of rays if the source is complicated enough to require

multiple point source approximations and the geometry has many cells requiring tracing along several rays each. Additionally, in a similar manner to the semi-analytic method, this method cannot naturally estimate a collision source of higher collision-count than first.

2.2.6 Mitigation Through Monte Carlo Coupling

In problems where ray effects are severe, such as localized source problems, the transport method of choice is often Monte Carlo since it does not suffer from ray effects. However, in regions of many scattering collisions Monte Carlo simulations become expensive as it must follow the particles to termination. A combination of Monte Carlo with S_N methods has been proposed where the first collision source simulated by a Monte Carlo code is fed into a discrete ordinates code in a similar manner to the point-kernel or analytic first collision source methods [23].

The method presented in [23] involves the usage of a Monte Carlo simulation, either multigroup or continuous energy, to create a first collision source for a discrete ordinates calculation to use as an "external" source. Like the semi analytic and point-kernel methods, this method involves splitting the problem based on particles' collision-count rather than by geometric or energy boundaries. Now though, the method for determining the uncollided flux is Monte Carlo rather than analytic or by ray tracing.

A problem is considered in [23] that is collision dominated, making it a prime candidate for discrete ordinates solutions, but containing important regions prone to severe ray effects. Such a problem would be expensive for a Monte Carlo simulation as the dominance of collisions may require tracking the particles through many scattering events before they are terminated. However, the low scattering material present in portions of the problem may cause catastrophic failure in the discrete ordinates calculation due to ray effects. An example of such a problem

could be a localized source in a room filled with air and a detector placed a distance away. The detector is collision dominated and would require many collisions to fully resolve in a Monte Carlo simulation, however the air separating the two would incur major ray effects in the transport process from the localized source to the detector. This motivates using Monte Carlo to calculate the first collision source and discrete ordinates to calculate the collided flux.

The method can be described through a derivation beginning with the original transport problem in Eq. 2.1. The flux is rewritten as

$$\psi(\vec{r}, E, \vec{\Omega}, t) = \psi_u(\vec{r}, E, \vec{\Omega}, t) + \psi_c(\vec{r}, E, \vec{\Omega}, t) \tag{2.9}$$

where ψ_u is the uncollided flux and ψ_c is the collided flux, then these fluxes satisfy,

$$\frac{1}{v}\frac{\partial \psi_u}{\partial t} + \vec{\Omega} \cdot \nabla \psi_u(\vec{r}, E, \vec{\Omega}, t) + \Sigma_t(\vec{r}, E)\psi_u(\vec{r}, E, \vec{\Omega}, t) = Q(\vec{r}, E, \vec{\Omega}, t) \tag{2.10}$$

$$\frac{1}{v}\frac{\partial \psi}{\partial t} + \vec{\Omega} \cdot \nabla \psi_c(\vec{r}, E, \vec{\Omega}, t) + \Sigma_t(\vec{r}, E)\psi_c(\vec{r}, E, \vec{\Omega}, t) = \int_0^\infty \int_{4\pi} \Sigma_s(\vec{r}, \vec{\Omega}' \to \vec{\Omega}, E' \to E)\psi_c(\vec{r}, E', \vec{\Omega}', t) d\vec{\Omega}' dE' + Q_u(\vec{r}, E, \vec{\Omega}, t) \tag{2.11}$$

respectively, where $Q_u(\vec{r}, E, \vec{\Omega}, t) = \int_0^\infty \int_{4\pi} \Sigma_s(\vec{r}, \vec{\Omega}' \to \vec{\Omega}, E' \to E)\psi_u(\vec{r}, E', \vec{\Omega}', t) d\vec{\Omega}' dE'$ and is referred to here as the first collision source. Equation 2.9 satisfies Eq 2.1 under conditions 2.10 and 2.11. Therefore, this provides a method of coupling the first collision source to the fully collided solution. Boundary conditions take the general form shown in Eq. 2.4. This makes the boundary condition for the new, coupled pair of problems,

$$\psi_u(\vec{r} \in \partial V, E, \vec{\Omega}, t) = \Gamma(E, \vec{\Omega}, t) \text{ for } \hat{n} \cdot \vec{\Omega} < 0 \tag{2.12}$$

$$\psi_c(\vec{r} \in \partial V, E, \vec{\Omega}, t) = 0 \text{ for } \hat{n} \cdot \vec{\Omega} < 0 \tag{2.13}$$

so that all incoming flux into the problem is assigned to the uncollided flux portion, and the collided flux is assigned vacuum boundary conditions. Note that Eqs. 2.12 and 2.13 are written

for an original problem with explicit boundary conditions. Implicit boundary conditions, e.g. reflective, would replace the right-hand sides of these equations with an expression involving ψ_u and ψ_c, respectively.

It is worth noting that Eq 2.10 has the form of a purely absorbing medium with a fixed distributed source and boundary conditions, therefore it can be solved analytically for simple geometries and sources. But for the general case it can be solved efficiently via a Monte Carlo simulation where a particle's history is terminated upon its first collision. Equation 2.11 can then be solved by the method of discrete ordinates using the solution from Eq 2.10 to build the first collision source. Such a solution would eliminate ray effects in the uncollided flux and facilitate calculation of the collided flux that is hopefully well distributed in collision dominated regions to be solved in a computationally efficient manner.

However, for a geometry that results in a localized first collision source, e.g. a shielded point source surrounded by air, ray effects may still afflict the collided flux in regions dominated by higher collided flux. This is because the first collision source will be heavily concentrated in the shield around the point source. In other words, severe ray effects are likely in the solution of Eq 2.11 as it is used to model neutron transport across the low scattering regions propagating from a first collision source localized in the source shield.

It is concluded that the method is conceptually simple and is best suited to a localized source problem with regions that are collision dominated. However even in such problems, secondary ray effects may still be a major concern in cases where the first collision source remains localized.

This method was tested using MCNP for the Monte Carlo simulation and TWODANT for the discrete ordinates calculation. A homogeneous cylinder with a point source in the center

was considered in r-z geometry, with an 8 mean free path height and 3 mean free path radius. The results from a S_{16} calculation were analyzed in a case with $c = 0.5$ for both a first collision source coupled calculation and a solo calculation in [23]. Results from a S_4 calculation in a case with $c = 1.0$ for both a first collision source coupled calculation and a solo S_4 calculation were also analyzed.

It was observed that the ray effects are less substantial for c=1.0 than c=0.5. This is the result of a scattering dominated region for the c=1.0 case, making the ray effects less severe even without first collision source coupling. With c=0.5 the first collision source is localized due to the high scattering, but the scattering is still not high enough to mitigate ray effects through flux redistribution. This demonstrates that the first collision source method can be frustrated by problems where the first collision source is very localized. In such problems higher collided flux may dominate regions where ray effects are prevalent and the elimination of ray effects in uncollided flux and the first collision source may not be sufficient.

2.3 BeRP Ball Experiment

2.3.1 BeRP Ball Experiments

The BeRP ball is a weapons grade plutonium sphere used in detector and criticality experiments [24]. The ball represents a fission neutron source that is subcritical under normal conditions. The sphere has a mean radius of 3.7938cm. The calculated density of the sphere is 19.604 g/cm^3 giving the plutonium a total mass of 4,483.884 g. The isotopic composition of the sphere when it was originally manufactured in 1980 is presented in Table 2.1 from [24].

Table 2.1: Isotopic Composition of BeRP Sphere in 1980.

Isotope	Mass Fraction
Pu238	0.020%
Pu239	93.74%
Pu240	5.95%
Pu241	0.269%
Pu242	0.028%
Am241	557 ppm

Given the composition, particularly the presence of a large amount of Pu240, the sphere serves as an effective subcritical spontaneous fission neutron source. As the sphere was manufactured in 1980, the composition has changed. An updated composition is available from 2009 detailing the change in isotopic composition of the sphere shown in Table 2.2 from [24]. It is this data that will be used for spontaneous source strength estimation in this work.

Table 2.2: Estimated BeRP Sphere Composition in 2009.

Constituent	Mass Fraction	Constituent	Mass Fraction
Pu238	0.016%	Mo98	2.2 ppm
Pu239	93.265%	Mo96	1.5 ppm
Pu240	5.907%	Zn66	1.4 ppm
Pu241	0.068%	Mo92	1.3 ppm
Pu242	0.028%	Cd111	1.3 ppm
Am241	2472.4 ppm	Cd110	1.2 ppm
Ga	335 ppm	Cd113	1.2 ppm
C	230 ppm	Pb206	1.2 ppm
U235	746.9 ppm	Pb207	1.1 ppm
U236	174.1 ppm	Be	1 ppm
Zr	100 ppm	B	1 ppm
Np237	77.8 ppm	Mg	1 ppm
Na	50 ppm	Cu	1 ppm
U234	39.2 ppm	Ag	1 ppm
Fe	10 ppm	Bi	1 ppm
Al	5 ppm	Zn68	0.97 ppm
Si	5 ppm	Mo100	0.90 ppm
Ni	5 ppm	Mo97	0.87 ppm
Sn	5 ppm	Mo94	0.81 ppm
Cr52	4.2 ppm	Cd116	0.77 ppm
Ca40	2.9 ppm	Cr53	0.48 ppm
Cd114	2.9 ppm	Cr50	0.21 ppm
Pb208	2.6 ppm	Zn67	0.21 ppm
Zn64	2.4 ppm	Cr54	0.12 ppm
Cd112	2.4 ppm	Cd106	0.12 ppm
		Balance	2860.3 ppm

The sphere is surrounded by a stainless-steel cladding of approximate thickness 0.0305 cm with a nominal density of 7.62 g/cm^3. This cladding has a flange extending around its center

of thickness 0.0914 cm. Additionally, a gap exists between the steel shell and the plutonium sphere expressed by the inner radius of the shell as 3.8278 cm. This gap also implies the sphere is sitting at the bottom of the spherical shell instead of being co-centric.

The BeRP ball is designed to be inserted into reflecting spherical shells. These shells act as both a moderating reflector that increases the induced fission rate produced in the ball, as well as a shield changing the spectrum and strength of the emitted neutrons that escape the reflector. The shells exist in a variety of sizes, with larger shells fitting around smaller shells to go from at least 0.5 inches to up to at least 6 inches. Shells also exist in a variety of materials including but not limited to high density polyethylene (HDPE) and copper.

In use since 1980, the BeRP ball has been featured in several experiments. One such experiment involves the use of the SNAP gross neutron counter [25]. This experiment expanded on the data accumulated by previous works and uses the Denovo 3D discrete ordinates code to simulate the subcritical system and compute sensitivities of the detector response function. The counter itself is composed of a polyethylene body with polyethylene top and bottom covers. Inside this cover exists a cadmium sleeve surrounding a polyethylene tube that covers a stainless steel tube holding the helium-3 where upon interaction by a neutron in a (n,p) reaction produces a count. The SNAP includes an optional removable HDPE shield that can be attached to the front of the detector. This shield serves to further thermalize incoming neutrons which in turn increase the number of neutrons absorbed by the cadmium tube, decreasing the total count rate. This serves to isolate the detector response to result from only fast neutrons that can survive the thermalization in the shield and subsequent termination in the cadmium sleeve.

Additionally, neutron multiplicity experiments involving the nPod multiplicity counter have been performed with the BeRP ball using various thicknesses of HDPE reflectors [26]. This

detector involves 15 helium detector tubes encased in a polyethylene body placed a distance away from the source. One of these studies has also involved simulation of the system using MCNPX-PoliMi, an enhanced version of MCNPX developed for simulating correlation measurements [26]. Such experiments have shown pretty good agreement between experimental measurements and simulated results.

Experimental work previously done with the BeRP ball shows precedent in using it as a benchmark problem for transport code models. The previous work also establishes a method for measuring the source and considering varying layers of reflective shielding as part of the experiment.

2.3.2 Experimental Models

Constructive solid geometry models for both the SNAP and nPod detectors as well as the BeRP Ball and an approximation of the experiment environment, such as the floor and the table, have been created in MCNP for the purpose of experiment simulation. These models contain geometric and material information, as well as information regarding the counting methods of the detectors. Schematics of these systems have been created and provide a more visual representation of the assemblies. Together a complete description of the geometry and material composition of the experimental setup can be obtained as well as methods of count calculation [27]. So, all the information necessary for a full system model has been created by previous simulation works.

Multigroup cross sections are also necessary for any discrete ordinates model. Multigroup cross sections can be obtained in a couple of different ways. Some multigroup data already exists in the form of libraries such as the WIMS-D library. However, many of these libraries are often created for the purpose of reactor simulations, and therefore may not always be the perfect fit for

detector and shielding applications. A more accurate method to create a benchmark model involves the use of the SERPENT Monte Carlo transport code. This code offers the capability to construct cross sections for given materials during a transport run [28]. These cross sections contain full information including out of group scattering and fission yields. They generate cross sections based on the interaction rates simulated in the environment with customizable region separations and energy group structure. Therefore, they are ideal for preserving reaction rates per Eq. 2.2 for benchmark problems since the flux spectrum used in their generation come from the exact system that is going to be modeled.

These multigroup cross sections can also be used effectively in MCNP to determine the validity of the generated multigroup cross sections [29]. Formats of the cross-section libraries that are suitable for MNCP have been documented in their application, allowing for effective use of MCNP multigroup simulations [30]. Such simulations allow for a more complete description of errors associated with the multigroup cross sections as an MCNP run does not encounter ray effects or meshing error.

Chapter 3. Experimental Campaign

The experimental stage of this project involved performing our own measurements with the BeRP Ball [24]. The experiments were conducted in the Device Assembly Facility (DAF) located at the Nevada National Security Site (NNSS) on August 3, 2017. These experiments involved the use of both the SNAP gross neutron counter [24], as well as the MC-15 multiplicity counter (a detector similar to the nPod [24]). The purpose of these experiments was to create a high-quality data set to use for the validation of the THOR transport code, including the mitigation of ray effects in the code through Monte Carlo coupling. The experimental results and computational model are also intended to serve as a benchmark for nonproliferation applications of transport codes. To this end the experiment was performed and data was gathered, recorded, and analyzed as described in this and subsequent chapters of this thesis.

3.1 Experiment Setup

The experiment setup involved the placement of the BeRP Ball source on a stand toward one side of a table with the SNAP detector sitting on the table facing the ball on one side, and the MC-15 detector sitting on the table facing the ball on the opposite side. The front of the SNAP detector was 1m from the centerline of the source-stand configuration and the front of the MC-15 was 0.5m on the other side. The table was made of aluminum and was approximately level. The table's width measured 77cm at the SNAP centerline and 76.5cm at the MC-15 centerline. The BeRP ball sat on an aluminum stand giving it a height of 22.2cm from the center of the source to the surface of the table. Fig 3.1 is a picture of the experiment setup.

Figure 3.1: Bare BeRP Ball experiment with optional polyethylene shield attached to the SNAP detector.

The experiment was also performed with various spherical reflectors surrounding the BeRP Ball. The reflectors used in separate experiments were 3 inches of high density polyethylene (HDPE), 1 inch of tungsten, and 1 inch of copper. For each of these cases though, different stands were used to maintain source mechanical stability. This resulted in the height of the BeRP ball varying slightly among the four experiments. The ball was 22.2cm, 22.5 cm, 22.1cm, and 22.3cm above the table's surface in the experiment with the bare ball, the HDPE, the tungsten, and the copper reflectors, respectively. Fig 3.2 shows the BeRP ball in the bottom half of the spherical HDPE shielding.

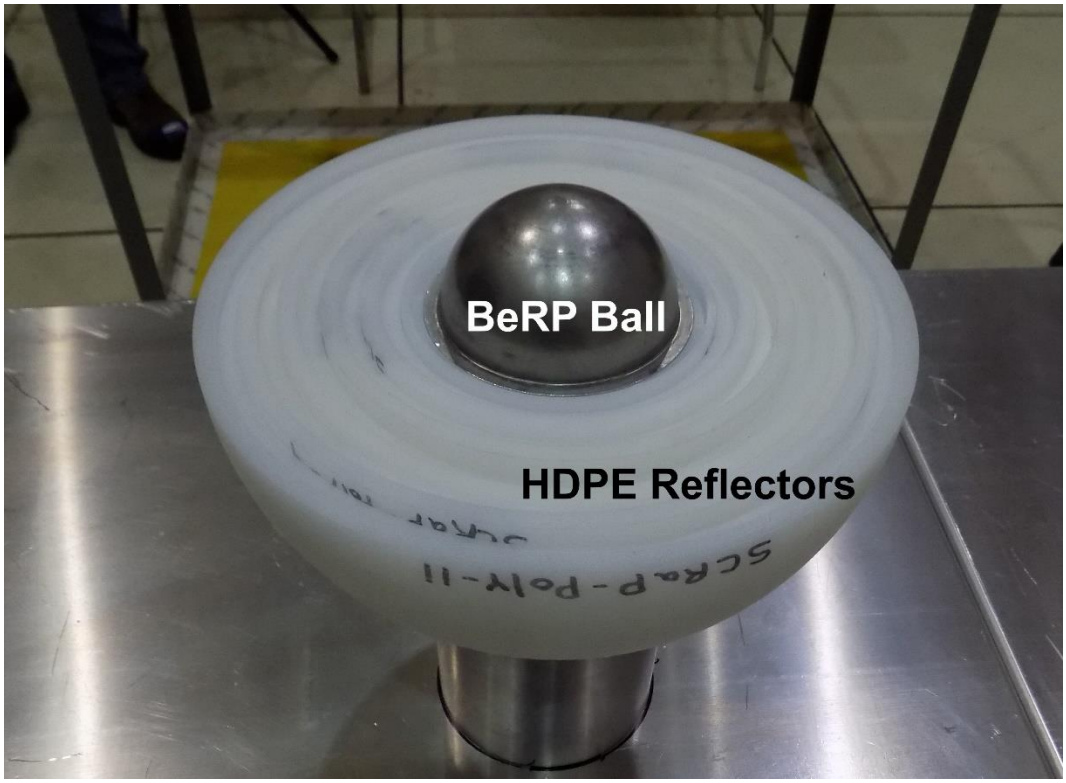

Figure 3.2: BeRP ball in the lower half of the HDPE reflector.

For each experimental case with reflectors, the measurement with the SNAP detector was executed for either 10 minutes or until 40000 counts had been registered, whichever came first. The minimum SNAP experiment run time was 4 minutes and 30 seconds as detailed below. The MC-15 was run for 10 minutes for every single case. Results from the MC-15 were transferred directly to a computer via wired connection, however the SNAP required recording the counts by hand after each experiment. It is unlikely that the occasional person going up to check on the SNAP status caused any discrepancy in experimental results. Each of these cases was performed twice, once with the HDPE shield covering the front of the SNAP detector, and once with it removed. It should be noted that the HDPE on the SNAP is hypothesized to have a negligible impact on the response of the MC-15. This then results in 8 total experiments performed with the SNAP detector, and 4 total experiments performed with the MC-15 detector. In addition, a

calibration experiment involving a californium source in place of the BeRP Ball was performed both with and without the SNAP HDPE shield with 20 minute runtimes each.

3.2 Experiment Results

Table 3.1 shows gross neutron counts from the SNAP detector for all experimental cases run.

Table 3.1: Experimental Results from the SNAP Detector.

SNAP Shield:	Yes			No		
BeRP Reflector	Time [s]	Counts	Count Rate [1/s]	Time [s]	Counts	Count Rate [1/s]
None	600	2.59E+04	43.13	600	3.18E+04	53.06
3'' Poly	600	2.84E+04	47.29	472	4.00E+04	84.76
1'' W	590	4.00E+04	67.80	450	4.00E+04	88.89
2'' Cu	582	4.00E+04	68.73	456	4.00E+04	87.75
Cf Calibration	1200	5.33E+03	4.44	1200	6.66E+03	5.55

As may be expected, the addition of the HDPE shield thermalizes the incoming neutron spectra and reduces the count rate in the detector for all measured cases as fewer fast neutrons survive attenuation in the SNAP's cadmium sleeve mentioned in Section 2.3.1. Reflectors on the BeRP Ball have two opposing effects on the count rate of the SNAP detector. The first is that the increase in moderation and reflection of the fission source increases the induced fission source, increasing the total source from the BeRP Ball which will in turn increase the count rate. However, the reflectors also thermalize the neutron spectrum exiting into the air. A more thermal spectrum will experience a greater attrition in the cadmium sleeve, which decreases the count rate. These two opposing factors do not equally cancel each other out in these experiments and it is observed that the reflectors used have a net positive effect on the count rate. Additionally, it is of note that 1 inch of copper and 1 inch of tungsten had almost the exact same effect on the count rate both with and without the SNAP's HDPE shield. Gross neutron count results for the MC-15 are shown in Table 3.2.

Table 3.2: Experimental results from the MC-15 detector.

SNAP Shield:	Yes			No		
BeRP Reflector	Time [s]	Counts	Count Rate[1/s]	Time [s]	Counts	Count Rate[1/s]
None	600	4893528	8155.88	600	4890504	8150.84
3'' Poly	600	8435796	14059.66	600	8414850	14024.75
1'' W	600	8364414	13940.69	600	8371176	13951.96
2'' Cu	600	8156976	13594.96	600	8171370	13618.95
Cf Calibration	1200	968460	807.05	1200	964164	803.47

It is evident from the results in Table 2.2 that the MC-15 detector's count rate does not change appreciably with the removal of the HDPE shield on the SNAP detector. This confirms our conjecture that the detectors are decoupled and do little if anything to alter the count rates of each other. A graphical representation of the measured count rates reported in Tables 3.1 and 3.2 can be seen in Fig 3.3.

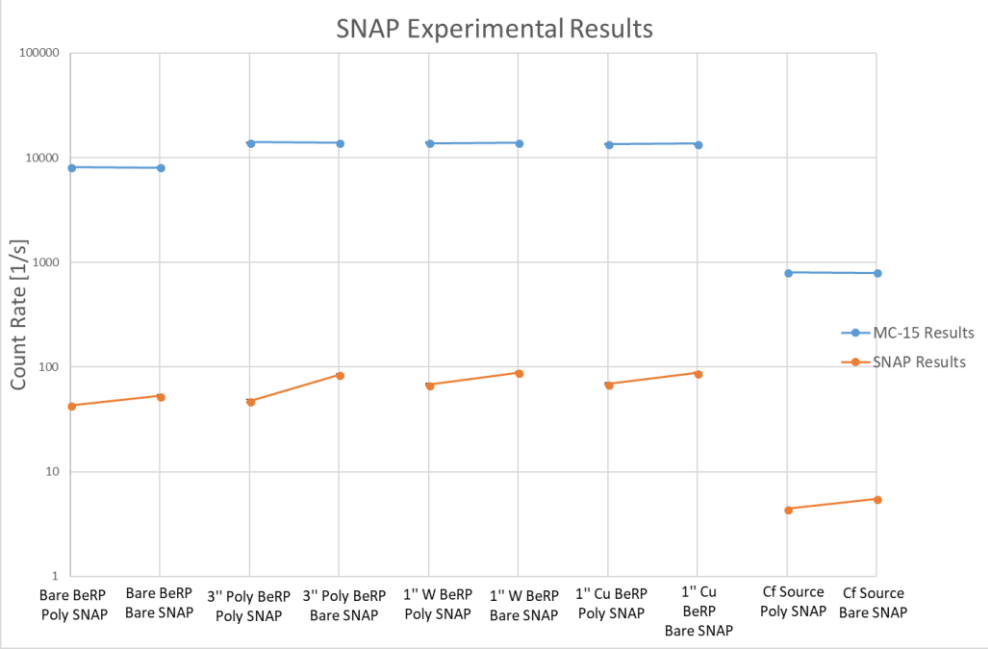

Figure 3.3: SNAP and MC-15 Results.

Chapter 4. MCNP Model Validation

4.1 Full Model of the BeRP Ball and the SNAP Detector

A full model of the SNAP detector and BeRP ball experiment was created in MCNP. This model was created using a reasonably detailed model of the SNAP detector, as well as a model of the experiment setup provided by Los Alamos. This model involved the full geometry of the SNAP, including the tripod stand and an approximation of the electronic circuitry of the detector.

For the experiment, the model included the BeRP ball as well as the steel shell and flange around it with the gap between them. The reflectors were likewise modeled including the gap necessary for the steel flange to fit in. The table was modeled as 3mm thick iron plate sitting 90.2cm above the floor. The BeRP ball was modeled as a 3.7938cm radius sphere 21.1582cm above the table with an aluminum stand holding it up. The SNAP detector was modeled as 107.5cm from its centerline to the ball-stand arrangement centerline (1m from the face of the detector to the ball-stand centerline) and 111.3582cm above the floor with respect to the front face center-point. The room was modeled as an air cylinder with no walls or ceiling, but with a concrete floor that was 45.72cm thick. The radius of the room was modeled as 8m from the origin, more than sufficient to fully encompass the detector and BeRP ball. The stand model was not changed for each different reflector. The full configuration boundary conditions were set to vacuum.

For a given mass of radioactive material, the rate at which neutrons are produced through spontaneous fission can be computed according to,

$$NR_{SF} = m_t \, N_A \, \ln 2 \sum_i \frac{w_i \, \gamma_{SF_i} \, \nu_{SF_i}}{M_i \, T_{1/2_i}} \qquad 4.1$$

where m_t is the total mass of the material in grams, and N_A is Avogadro's number. The rest of the quantities in Eq. 4.1 are specific to isotope *i* such that w_i is the isotopic weight percent, γ_{SF_i} is the fraction of decays that are spontaneous fissions, ν_{SF_i} is the average neutron yield per spontaneous fission, M_i is the atomic mass in grams per mole, and $T_{1/2_i}$ is the half life in seconds. This allows the spontaneous fission neutron production rate, NR_{SF}, to be computed in units of sec^{-1} for the BeRP ball which has a mass of 4483.884 grams with isotopic abundances listed in Table 2.2. Table 4.1 shows this calculation (decay and atomic mass data were obtained from the Korea Atomic Energy Research Institute (KAERI) website [31]).

Table 4.1: Spontaneous Fission Neutron Production Rate of BeRP ball.

Isotope	M_i	w_i	T_1/2_i	gamma_SF_i	nu_SF_i	NR_SF
Pu238	238.0495534	0.02%	2.7657E+09	1.8000E-09	2.28	1.8667E+03
Pu239	239.0521565	93.27%	7.6002E+11	4.4000E-12	2.16	9.1314E+01
Pu240	240.0538075	5.91%	2.0716E+11	5.0000E-08	2.21	2.4567E+05
Pu241	241.0568453	0.07%	4.5254E+08	5.7000E-15	2.25	1.4963E-01
Pu242	242.0587368	0.03%	1.1858E+13	5.5000E-06	2.24	2.2495E+03
Am241	241.0568229	0.25%	1.3674E+10	4.1000E-12	3.22	1.8534E+01
Total						2.4989E+05

This rate is dominated by neutrons from Pu240, for this reason the continuous energy spectrum used for spontaneous fission neutrons is that of Pu240 described by the Watt fission spectrum in Eq 4.2 and shown in Fig 4.1.

$$p(E) = Ce^{\frac{-E}{0.794930}} \sinh(4.68927\ E)^{1/2} \qquad 4.2$$

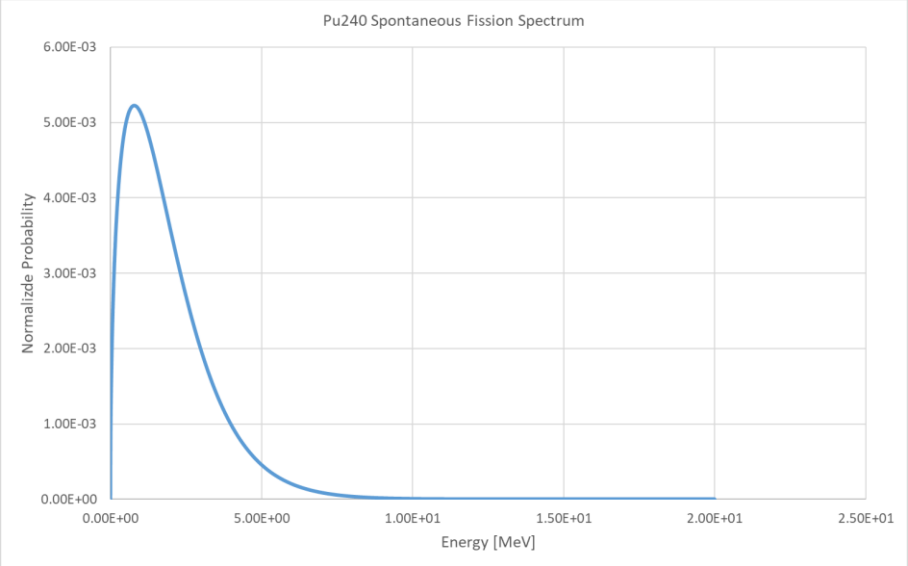

Figure 4.1: Pu240 Spontaneous fission spectrum normalized over 20 MeV.

Spatially the source was evenly distributed throughout the plutonium in the BeRP ball. The method of registering counts in the detector was by multiplication of the neutron scalar flux in the active portion of the helium-3 tube by the (n,p) reaction cross section of the helium and the active volume of the helium. This yields (n,p) reaction rates which should be equal to the count rate in the SNAP detector.

4.1.1 Validation of the Full Model and Error Quantification

Count rates computed via the full MCNP model are shown in Table 4.2 where the Count Rate is obtained by multiplying the corresponding Counts Per NPS entry with the Spontaneous Fission Neutron Production Rate computed in Table 4.1.

Table 4.2: MCNP Results for the Full SNAP Model.

Case	Counts Per NPS	Count Rate [1/s]	Uncertainty [%]
Bare BeRP Poly SNAP	0.000147164	36.77510629	3.19%
Bare BeRP Bare SNAP	0.000175303	43.80681728	2.91%
3'' Poly BeRP Poly SNAP	0.000176281	44.05121165	2.97%
3'' Poly BeRP Bare SNAP	0.000315167	78.75771196	2.17%
1'' W BeRP Poly SNAP	0.000284552	71.10726838	2.32%
1'' W BeRP Bare SNAP	0.000387261	96.77342581	1.97%
1'' Cu BeRP Poly SNAP	0.000255212	63.7754371	2.43%
1'' Cu BeRP Bare SNAP	0.000336874	84.18211761	2.14%

Validation of the MCNP full model is shown in Fig 4.2 by comparing the computed to experimental rates for the various BeRP-reflector and SNAP-shield combinations.

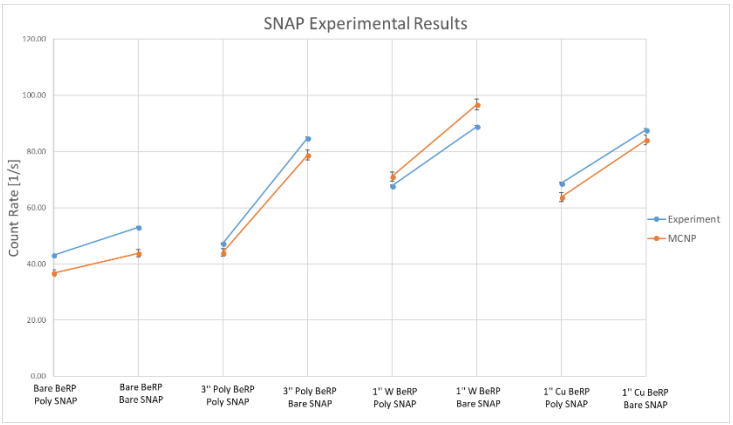

Figure 4.2: MCNP vs Experimental Count Rates for SNAP detector.

Error bars are included in this plot; however, they are quite small and mostly not discernible on the utilized scale. It can be seen that the experimental results do indeed differ from the MCNP simulation results. In almost all cases the experimental results are larger than their computed counterparts, except in the case of the tungsten reflector experiment where the MCNP simulation overestimates the count rate. The cause of this exception in the trends is not known. It can be seen though that the general trend where including the reflectors increases the count rate while the shield decreases it is still observed by both the experiment and simulation count rates.

The absolute relative error (ARE) of the MCNP calculation *versus* the measured values is depicted in Fig 4.3.

Figure 4.3: Absolute Relative Error with respect to the measured values in SNAP's Count Rates Computed by MCNP Simulations Using the Full Model.

The error in the simulation for all cases is bounded below 20%. In fact, the highest relative error occurs in the *Bare BeRP Bare SNAP* case, where the error is 17.4%. This case along with the 14.7% error case for *Bare BeRP Poly SNAP* attain the two highest errors, and the two most important since much of the rest of this work will focus on these two cases. The error for all the other cases is bounded below 9%, but it must be noted that all these errors far exceed MCNP's statistical errors reported in Table 4.2.

The error in the simulation may arise from a variety of issues. Firstly, a Monte Carlo simulation must rely on tabulated cross section data which will always incur some measure of error. Secondly, the simulation geometry does not conform exactly to the experiment setup. The most substantial of these differences include the lack of walls and ceiling. Information on walls and ceiling dimensions is not provided for the building in the DAF where the experiment was performed but would likely have a measurable effect on the simulation since the floor model was

found to be influential as will be discussed in the next section. The detector is also not quite at the right height being even with the center of the ball in the simulation and the ground is slightly further away than in the experiment. Finally, the determined spontaneous fission rate is based on isotopic data that is about 8 years old via decay data that has error inherent in it.

What can be said for certain though, is that the total error in the simulation of the experiments is less than 20% for all cases run. The count rates from the simulation are approximately the same as from the experiment, with some being within 5%.

4.2 Simplified Model of the BeRP Ball and the SNAP Detector

Due to the nature of tetrahedral meshes, certain elements of the experiment's configuration can be difficult, if not impossible, to model accurately. Thin sleeves or the like compared to a large object may not be possible to fully resolve in a tetrahedral mesh. For this reason, a simplified model of the experiment was created for later use in creating a THOR tetrahedral-mesh representation of the experiment setup. This model would serve as the basis for the THOR model and would provide a benchmark result to compare THOR calculations to. The sought model would strive to be as simple as possible while also providing an accurate representation of the BeRP Ball and the SNAP detector counting experiment.

The simplified model is composed of a plutonium ball the same size as the BeRP ball suspended in air 1m away from the nearest face of the detector. This detector is midlevel with the ball and is a simplified version of the full SNAP detector. The detector is comprised of an inner helium-3 tube with both lower and upper dead regions bordering a middle active region. This tube is surrounded immediately by a polyethylene sleeve which in turn is surrounded by a cadmium sleeve; the thin steel casing of the helium gas is forgone in this model. The cadmium sleeve is twice as thick as in the original model to facilitate meshing into reasonably shaped

tetrahedra with aspect ratios not too far from one and is modeled at a reduced density to preserve total nuclide content. Likewise, the polyethylene sleeve is made denser to preserve the total nuclide content between the cadmium sleeve and the helium tube. This assembly is then in turn contained in the detector body composed of polyethylene. This includes a surrounding semicircle and top and bottom poly covers. A variation with and without the poly shield can be created. An exploded view of the detector modeled in SolidWorks [32] without the poly shield is shown in Fig 4.4.

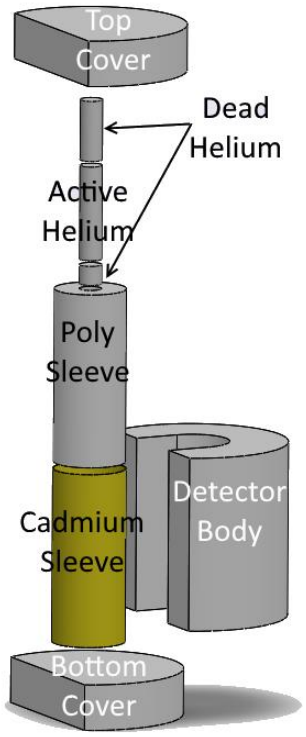

Figure 4.4: Simplified SNAP Detector Model in SolidWorks.

Dimensions of the simplified SNAP detector Model are presented in Table 4.3.

Table 4.3: Simplified SNAP Dimensions.

Piece	Height [cm]	Diameter [cm]	Cutoff from Center [cm]	Volume [cm^3]
Top Cover	4.928	20.320	4.775	1258.889
Upper Dead Helium	6.513	2.388	-	29.158
Active Helium	10.160	2.388	-	45.489
Lower Dead Helium	2.060	2.388	-	9.223
Poly Sleeve	18.733	7.198	-	678.477
Cadmium Sleeve	18.733	7.828	-	899.185
Detector Body	18.733	20.320	4.775	3634.671
Bottom Cover	4.928	20.320	4.775	1258.889

Here the cutoff from the center is the flat faces in the detector parts seen in Fig. 4.4. Diameters listed are outer diameters, inner diameters of tubes are found by comparing the connection between each part in Fig. 4.4. All parts are coincident. Additionally, note that the detector body has a cutout with width of its inner diameter to the end of the detector.

In addition, the full experiment setup was reduced from the full cylindrical room with the stand, table and floor described in Section 4.1, to just the air between the BeRP Ball and the detector. All this created a smaller and simpler model, which allows for faster analysis in addition to making the tetrahedral mesh generation possible. The simplified model is depicted as it was modeled with SolidWorks in Fig. 4.5.

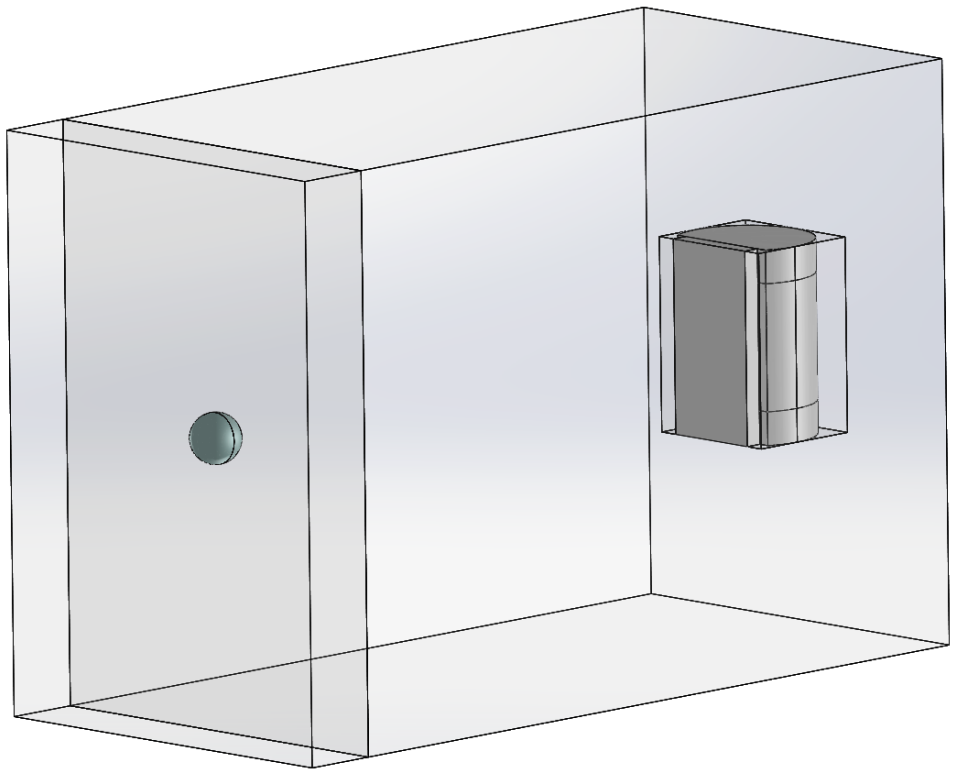

Figure 4.5: Simplified Experimental Model in SolidWorks.

The air box is 85.76cm from bottom to top, 60.96cm across, and 128.77cm long. This leaves a space of 7.3944cm of air between the edge of the BeRP ball and the edge of the air configuration near it. The circular back edge of the SNAP detector is coincident with the edge it is near.

4.2.1 Numerical Validation of the Simplified Model and Error Quantification

Reducing the complexity of the computational model in turn reduced the accuracy of the results. Each simplification to the model was recorded and the accumulated error quantified. This analysis was performed for the case with bare BeRP Ball measured with the SNAP without the HDPE shield. Table 4.4 shows the absolute relative error (ARE) introduced into the model by each simplification made. In this Table features included in the Full Model described in Section 4.1 are removed one by one and the count rate is reported together with the ARE compared to the previous simplification's count rate.

Table 4.4: Error introduced by simplifications to the full model.

Simplification	Count Rate	ARE Introduced
Full Version	43.80681728	NA
Floor Removed	40.58970767	7.34%
Tripod Removed	40.24910487	0.84%
SS Tube Removed	42.53211818	5.67%
Aluminum Housing Removed	43.22157021	1.62%
SS Shell Removed	41.9131357	3.03%
Table and Stand Removed	40.67866922	2.95%
Simplified Version	41.88339855	2.96%

Clearly significant cancellation of errors occurs, resulting in the final simplified model count rate only differing by 4.39% from the full model's value (43.8 *vs* 41.9). Removal of the floor is clearly the largest source of error in the simplified model. This large change in the count rate may also explain some of the error present in the full version compared to the experiment as even the full version lacked the room's walls and ceiling. Removal of these features was justified in that it made the problem substantially smaller and faster to run with less that the 20% error already present in the full model's results compared to experiment. It is also worth noting that all ARE's reported in Table 4.4 are only two to three times larger than MCNP's statistical uncertainties reported in Table 4.2.

The tripod holding up the detector was removed because it had very little impact on the result and was not trivial to model. The stainless-steel tube had the next largest impact after the floor. Removal of this piece was necessary as it was far too thin to be accurately modeled tessellated for THOR's purposes. The aluminum housing for the detector clearly made very little impact on the count rate and was geometrically a complicated component of the detector. The stainless-steel shell around the BeRP Ball made a somewhat significant difference in the computed value, however the shell and flange were too thin to be accurately modeled on a

tetrahedral mesh. Removal of the table and stand was justified in a similar manner to the removal of the floor and introduced a small error.

The final simplification to the cumulatively simplified model involved lining the detector up exactly with the ball in order to increase symmetry in the problem, as well as increasing the thickness of the cadmium shield to allow for it to be modeled by tetrahedra (while it was physically too thin, it is optically very thick in the thermal energy range, hence crucial to obtaining accurate (n,p) reaction density-rates in the Helium-3). To this end this version also featured an inner sleeve version of the polyethylene tube that is higher in density to make up for the thicker cadmium, which likewise had its density reduced, in order to preserve total mass of both.

All cases run with MCNP using the simplified version of the model are shown in Table 4.5.

Table 4.5: Simplified Model Count Rates Computed by MCNP.

Case	Counts Per NPS	Count Rate [1/s]	Uncertainty [%]
Bare BeRP Poly SNAP	0.000134195	33.53425694	3.30%
Bare BeRP Bare SNAP	0.000167606	41.88339855	3.07%
3'' Poly BeRP Poly SNAP	0.000240727	60.15575148	2.57%
3'' Poly BeRP Bare SNAP	0.000416056	103.969066	1.94%
1'' W BeRP Poly SNAP	0.000268897	67.19520912	2.37%
1'' W BeRP Bare SNAP	0.000360923	90.19177032	2.06%
1'' Cu BeRP Poly SNAP	0.000237456	59.33835475	2.49%
1'' Cu BeRP Bare SNAP	0.000290757	72.65784824	2.26%

It is seen that for the most part, the count rates and uncertainties are similar to those of the full version presented in Table 4.2. A more direct comparison can be made by plotting the results against each other as depicted in Fig 4.6.

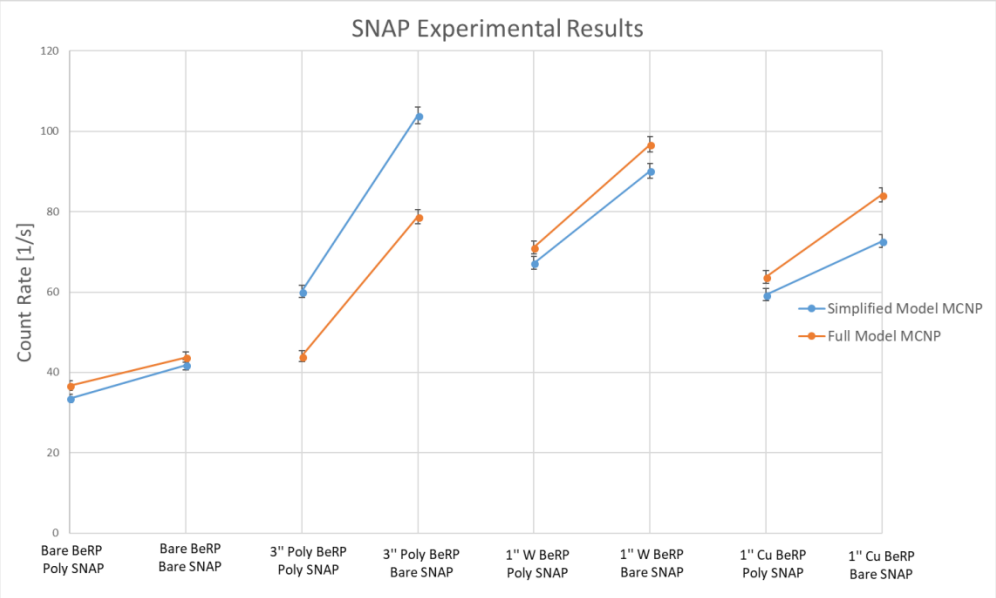

Figure 4.6: Comparison of Simplified and Full Model Count Rates.

Fig 4.6 shows that by far the largest error occurs in the comparison of the experiments involving the 3-inch HDPE reflector, and the lowest error is incurred in the bare BeRP Ball case. It is the bare BeRP Ball case that will be the focus of the rest of this work and the model used hereon will be the simplified model, so these results should be kept in mind as the benchmark results that we are trying to achieve.

Chapter 5. Coupled Model Development

Development of the coupled method and model for THOR S_N with Hammer Monte Carlo involved creating a number of auxiliary functions and capabilities. External source multiplication was added to THOR to enable a more complete source specification for subcritical systems. A new flux visualization software system was introduced that involved slice snapshots to better visualize 3D ray effects and their subsequent mitigation. A method for generating THOR-compatible meshes with the popular CAD software SolidWorks [32] was implemented to make model development for THOR easier and more automated. Multigroup cross sections were generated by SERPENT [28] and a converter was made to allow for efficient translation of SERPENT-produced cross sections to THOR, Hammer, or MCNP formats. A converter for MCNP CSG input into Hammer input format was developed with limited capabilities (i.e., MCNP has a much wider range of object shapes compared to Hammer's more limited selection of shapes). Additionally, a method to feed Hammer's collisional source output into THOR as the external source input was designed and implemented. Finally, once all modules and capabilities were introduced, a model of the BeRP Ball in a box of air was created for a THOR mesh to allow for visual representation of ray effects and their subsequent mitigation. Similarly, the simplified SNAP model was tessellated as a THOR mesh to show the practical impact of ray effect mitigation on measurable quantities, e.g. count rates.

5.1 Subcritical Multiplication for External Source Problems

The current version of THOR can run in two different solution modes, both making use of the discrete ordinates method to solve the steady-state multigroup transport equation using the method of short characteristics [11]. The first is the criticality mode where the eigenvalue problem of a system is solved to determine the critical state of the system. This method involves

a zero external source and starts the iterative process with a non-zero flux-moments guess throughout the physical domain to determine the source of secondary particles via fission and scattering to calculate a new iterate of the flux and eigenvalue (k_{eff}) via a set of external source problems. The resulting new flux is then normalized and k_{eff} is updated. This process is repeated until the error in the flux and k_{eff} values is reduced to some pre-specified tolerance (the error is estimated by the maximum absolute change in each of the values between two consecutive iterations). The converged value of k_{eff} determines the critical state of the system, and the converged flux represents the fundamental mode. The second option in THOR involves solution of the transport equation for an external source problem per Eq 2.1. This method previously only incorporated scattered secondary particles in the production cross section on the right-hand side of Eq. 2.1 that is then solved via standard inner and outer iterations. Because external source problems sometimes involve multiplication through fission reactions, this equation must be altered to fully capture the physics of the system. Considering a system with isotropic scattering and fission, this prompts a desire to determine a solution to,

$$\begin{aligned}&\left[\vec{\Omega}\cdot\nabla+\Sigma_s(\vec{r},E)+\Sigma_a(\vec{r},E)\right]\psi\left(\vec{r},E,\vec{\Omega}\right)\\&=\frac{1}{4\pi}\int d\vec{\Omega}'\int dE'\,\Sigma_s(E'\rightarrow E;\vec{r})\psi\left(\vec{r},E',\vec{\Omega}'\right)\\&+\frac{\chi_f(E)}{4\pi}\int d\vec{\Omega}'\int dE'\,\nu_f\Sigma_f(E',\vec{r})\psi\left(\vec{r},E',\vec{\Omega}'\right)+S\left(\vec{r},E,\vec{\Omega}\right)\end{aligned}\qquad 5.1$$

Here $\chi_f(E)$ is the fission energy spectrum with the assumption that the spectrum of fission produced neutrons is independent of incident neutron energy. There are two methods to accomplish this goal. The easiest method involves the addition of the fission production coefficients into the scattering cross section. Consider a multigroup scattering matrix that is transformed per the formula,

$$\tilde{\tilde{\Sigma}}_{s_{g'\to g}}(\vec{r}) = \Sigma_{\mathrm{s_{g'\to g}}}(\vec{r}) + \chi_{f_g}\nu_f\Sigma_{f_{g'}}(\vec{r}) \tag{5.2}$$

This effectively includes fission production without the need for algorithmic change to the method calculating the flux. For a more general approach though, it is possible to implement an extra calculation to add the fission contribution to the production term. This approach allows for simpler implementation of anisotropic scattering and is additionally just cleaner with respect to solving the transport equation. This then results in two different, but equivalent, multigroup equations for these two options. Equation 5.3 shows the option using the altered scattering matrix and is equivalent to Eq. 5.4 which is the standard form with scattering and fission production separated.

$$\left[\vec{\Omega}\cdot\nabla + \Sigma_{t_g}(\vec{r})\right]\psi_g(\vec{r},\vec{\Omega}) = \frac{1}{4\pi}\int d\vec{\Omega}' \sum_{g'=1}^{N_g} \tilde{\tilde{\Sigma}}_{s_{g'\to g}}(\vec{r})\psi_{g'}(\vec{r},\vec{\Omega}') + S_g(\vec{r},\vec{\Omega}) \tag{5.3}$$

$$\begin{aligned}\left[\vec{\Omega}\cdot\nabla + \Sigma_{t_g}(\vec{r})\right]\psi_g(\vec{r},\vec{\Omega}) &= \frac{1}{4\pi}\int d\vec{\Omega}' \sum_{g'=1}^{N_g} \Sigma_{\mathrm{s_{g'\to g}}}(\vec{r})\psi_{g'}(\vec{r},\vec{\Omega}') \\ &+ \frac{\chi_{f_g}}{4\pi}\int d\vec{\Omega}' \sum_{g'=1}^{N_g} \nu_f\Sigma_{f_{g'}}(\vec{r})\psi_{g'}(\vec{r},\vec{\Omega}') + S_g(\vec{r},\vec{\Omega})\end{aligned} \tag{5.4}$$

For the purposes of THOR, the second method was implemented to allow more general solutions for problems with anisotropic systems. However, the correctness of the implementation was verified by comparing results against the first method which could be implemented without any change to the underlying code, i.e. the original implementation without subcritical fission enabled. The results were compared through a subcritical BeRP Ball with HDPE reflector problem composed of 26,849 cells and showed a maximum absolute difference in the converged flux between 3.471E-08 and 5.285E-08 in the cell-averaged scalar flux, nearly three orders of

magnitude smaller than the defined convergence criterion of 10^{-5}. This equivalence of flux verified proper implementation of subcritical multiplication in THOR's external source option.

It must be noted here that if the problem configuration, i.e. size and isotopic densities, happen to be supercritical the flux iterates will continue to grow without limit and the problem will not converge since such configuration does not have a steady state solution. This can be monitored and detected by observing the relative change in each iteration leveling off to a value well above the convergence criteria. For this reason, loose convergence criteria are discouraged for external source problems with fission multiplication enabled since the change over each iteration for a non-convergent supercritical problem may level off at a smaller ratio than a loose convergence criteria and wrong results may then go undetected.

5.2 Flux Visualization Method

A method was devised to allow for visualization of THOR output flux results for a rectangular model. The method involves taking planar slices across the domain and plotting the flux at each slice allowing for flux visualization at varying locations in the domain. The visualizer consisted of three different options, each with their advantages and disadvantages. The first and recommended option involved parsing the flux to create exact resolution of each pixel of the image based on point locations in the tetrahedra. This is done by systemic sampling of a 3D mesh of points based on a user defined slice resolution and number of slices. These points are then tested for existence in each cell until all points have been assigned cell. This option was by far the most resource intensive for the parsing portion (though this is mitigated through parallel processing using OpenMP), however it is the most accurate plotting method. Once the parsing is finished, the plotting is performed by the Python or Matlab script and is relatively fast. An example result from this method is illustrated in Fig 5.1.

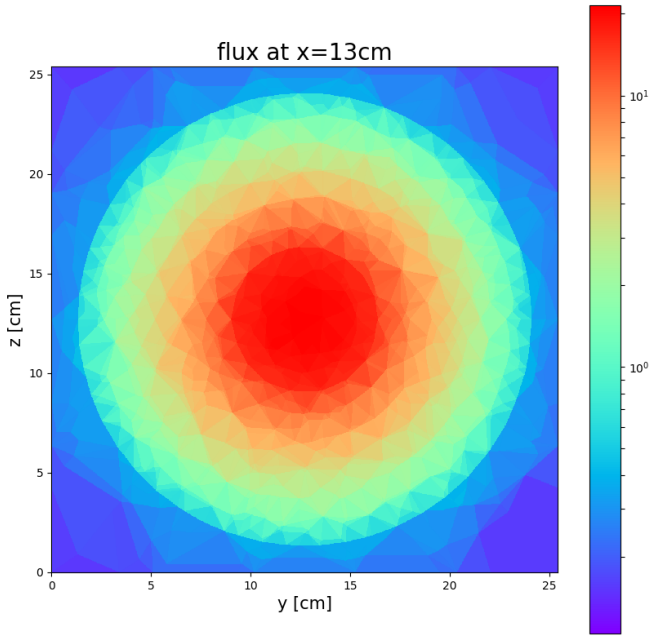

Figure 5.1: Fast flux plotted using option 1 of the visualizer for the BeRP Ball in HDPE Shell.

The second option involves mapping the flux of each tetrahedron to its geometric center. The mapped flux is then plotted using a Matlab script using the natural fitting option. This option is extremely cheap to parse; however, the plotting script is very resource intensive due to the natural fitting formula. This method results in a very smooth flux profile to give a visually appealing picture of the general flux trends in the given system, though it is less accurate compared to option 1 since it does not attempt to resolve each tetrahedron exactly, but rather to use the center of each tetrahedron to create a smooth gradient of flux. It can still be quite accurate in problems with extremely fine meshes as demonstrated in Fig 5.2.

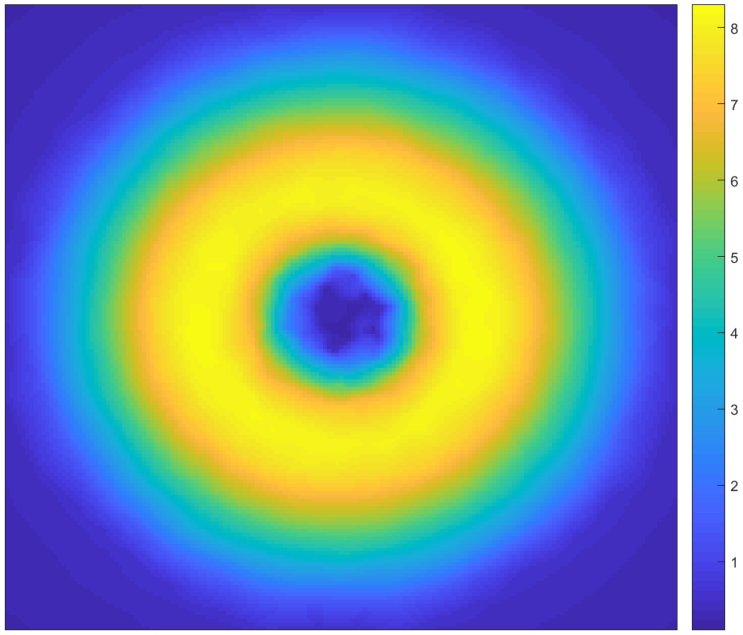

Figure 5.2: Thermal flux plotted using option 2 for the BeRP Ball in HDPE Shell.

The third option involves mapping of the flux to the center and near the corners of each tetrahedron in the mesh. This mapped flux is then plotted using nearest neighbor fitting on a new mesh in Matlab. This gives most points the correct flux for the cell they are in. The points will not all have the correct flux, and some may instead have flux from tetrahedrons next to the one they are actually in. While the parsing is marginally more expensive than option 2, it is comparable and still runs faster than option 1. The plotting mechanism is far faster than option 2 but not quite as fast as option 1. This leads to this method being by far the least expensive option overall, however the results are far less visually appealing than the other two options and also far less accurate than the results of option 1. This leads to this method only being recommended as an inexpensive visualization tool of the flux distribution and is not recommended as a publishable quality product. An example of this method is shown in Fig 5.3.

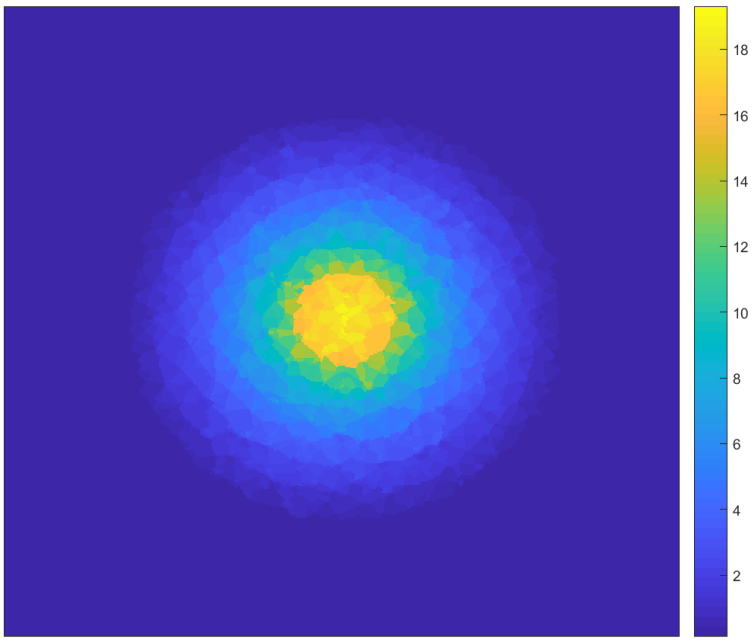

Figure 5.3: Fast flux plotted using option 3 for the BeRP Ball in HDPE Shell.

5.3 Mesh Generation Method using SolidWorks

SolidWorks [32] is a commonly used CAD (Computer Assisted Design) program employed by engineers and designers. The program is intuitive in its use and similar in function to many other popular CAD programs such as AutoCAD [33]. It also contains meshing capabilities for solid-body models created in the program. This capability includes tetrahedral meshes, of the kind that are used in THOR. Additionally, there exists capabilities for mesh refinement on different parts or portions of the geometry to allow for more important regions to be modeled more finely. For these reasons, we chose to use SolidWorks to create THOR compatible meshes of the problem geometries for the test and validation cases examined in this work. Example SolidWorks solid-body models were shown in Fig 4.4 and 4.5 and a representative mesh generated in SolidWorks for the BeRP Ball and reflector is shown in Fig 5.4.

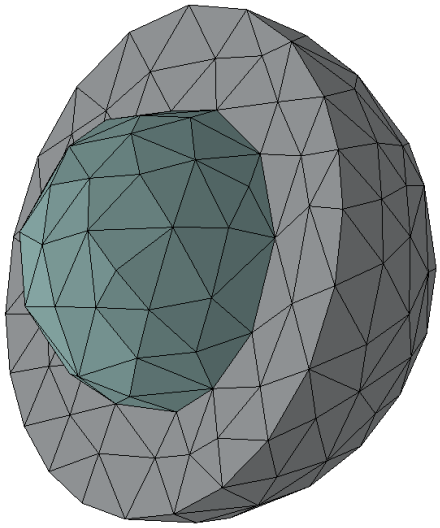

Figure 5.4: BeRP Ball in Reflector Tessellated with SolidWorks.

Fig 5.4 also demonstrates the inability of a tetrahedral mesh to fully resolve curved geometries. The finer the mesh the more accurate the representation of curved surfaces and the better the conservation of their enclosed volumes, however it is generally impossible to fully preserve the shape using tetrahedrons. For this reason, examination of region volumes is often essential in such meshes since an increase in an influential volume/material, like say the plutonium sphere, may result in discrepancies such as a source strength that is scaled up/down depending on the sense of volume non-conservation compared to the true, un-discretized model. Such inconsistencies in volumes should be noted and considered as potential sources of error in so-computed results.

5.3.1 Converter from UNV format to THOR Mesh

Meshes generated with SolidWorks can be output to the UNV format developed by Structural Dynamics Research Corporation (SDRC) [34]. This format contains information on problem configuration, from material properties like density and stress constants, to mesh information like tetrahedral vertices. The files contain all information necessary to create a THOR compatible mesh. The format was originally converted to the more common GMESH

format [35] through the finite element code libMesh [36]. GMESH already could be converted to THOR through the existing THOR format converter. However, for our purposes and future utility of THOR it was decided that it would be far simpler and more convenient to convert the mesh directly from UNV format to THOR format. To this end a new converter capability was added to the THOR Mesh Generator utility. Such capability allows any user a fast and intuitive means of converting from UNV mesh output generated by SolidWorks directly to a THOR compatible mesh.

5.3.1.1 Boundary Conditions

The only missing information in the UNV format that is necessary for a THOR compatible mesh is which faces belonging to which tetrahedra are problem boundary faces. Fortunately, this information can be determined through calculation of tetrahedra adjacencies. The simplest general method of doing this involves comparing the vertices of each face of each tetrahedron to the vertices of each face of all other tetrahedra. If a match is not found, then the tetrahedron has no adjacent cells on that face and the face is flagged as a boundary face. This is the most resource intensive portion of the format conversion since the information is not already known, however it can easily be parallelized for each tetrahedral cell. For the largest meshes tested with this method, upwards of 200,000 cells, the process still only required a few seconds using 16 processor cores to determine all boundary faces.

5.3.1.2 Material Tracking

The UNV mesh generated by SolidWorks contains information as to what material each cell is composed of, however the information is in the form of real valued properties of the material, e.g. density. Unfortunately, these properties do not contain the names of materials recorded in their information set and the ordering does not seem to correspond to the order that

parts composed of that material are introduced into the global configuration. However, their information set contains material data information such as density and stress constants. This leads to two different methods of determining what material corresponds to which numerical value. The original method used for simple problems was comparison of volume information of the cells with the known volume of the objects in the problem configuration. However, as objects became more complicated this method proved prohibitive since regions span all parts of a given material type, so for example the total volume of all polyethylene from Fig. 4.5 would need to be calculated and summed then compared to the volume of the cells of each region to determine which region represented polyethylene. This difficulty was solved by instead examining UNV files for material data corresponding to a given material. For example, a material whose UNV file assigns a density of 1.1E-6 kg/cm^3 would be identified as air. The easiest practical way to do this, and therefore the recommended method, is to define custom materials and map their custom densities to their corresponding materials. For instance, the plutonium comprising the sphere may be mapped to a fictional density of 239 kg/cm^3. Since THOR does not make use of any of this material information, changing the properties has no effect on the mesh except tagging various materials.

5.4 SERPENT Cross Section Generation

As described in Section 2.3.2 SERPENT has the capability to generate multigroup cross sections using a Monte Carlo simulation of the underlying physics [28]. These cross sections permit general-order anisotropic scattering and although THOR can make use of anisotropic scattering information, for the purposes of this work scattering was limited to isotropic in all tested cases. Normally, simplified sub-models with homogeneous regions are used to create multigroup cross sections in SERPENT for complicated configurations where the full geometry

may be very difficult to run in Monte Carlo. However, since the purpose of this work is to examine ray effects and create a neutron detection benchmark problem for discrete ordinates methods, the generation of multigroup cross sections was performed using the same simplified model representation presented in Section 4.2.

5.4.1 Multigroup Cross Section Format Converter

SERPENT cross sections come in a format that is not compatible with THOR's native format. For this reason, a cross section converter THORxsGen was created to allow for automated transformation of SERPENT multigroup cross sections to a format that is compatible with THOR. Since the structure of the cross-section converter was already in place, it was determined that the code would be expanded to include the capability to begin with THOR or SERPENT formatted multigroup cross sections and output the data to either THOR, MCNP, or Hammer compatible formats. The resulting code enabled the conversion from all cross-section formats we commonly possess, to all formats we desired to use. Expansion of the conversion code is simple for anyone with adequate information about both their input or output format of choice as the structure already exists and is well documented.

5.5 Hammer to THOR Coupling Method

Coupling of the discrete ordinates transport code THOR with the Monte Carlo neutron transport simulator Hammer is based on the uncollided flux coupling method described in Section 2.2.6. The method is expanded to work for a general $(n-1)$-collided flux and n-collided source for problems where ray effects may persist past the uncollided flux. Supporting software application of the method through was created to allow easy coupling between Hammer output and THOR input.

5.5.1 General Collision-count MC/S_N Coupling Derivation

Monte Carlo simulations do not require an angular discretization and therefore do not experience ray effects, making them well-suited for problems where this issue is present. While solutions from the Monte Carlo method are the most accurate, obtaining them is often more computationally expensive than S_N methods, which motivates a hybrid approach.

The proposed method is to use Monte Carlo simulations to solve for the low collision-count flux in problem areas of the domain (killing the simulated particle after a certain number of collisions) and use S_N methods to solve for the fully collided flux. Our new method is formulated as follows.

The linearized steady state radiation transport equation can be expressed in operator form as,

$$\mathbf{L}\psi = \mathbf{S}\psi + \mathbf{Q} \tag{5.5}$$

where **L** is the collision and streaming operator in the transport equation acting on the angular flux ψ, **S** is the secondary (scattering and fission) production operator, and **Q** is the external source. Here vacuum boundary conditions are assumed, but this is not essential for the formalism. The angular flux ψ can be written as the infinite series,

$$\psi = \sum_{i=0}^{\infty} \psi^{(i)} \tag{5.6}$$

where $\psi^{(i)}$ is the flux of particles that have experienced exactly i collisions. Operator splitting leads to a set of equations in $\psi^{(i)}$,

$$\mathbf{L}\psi^{(0)} = \mathbf{Q} \tag{5.7}$$

$$\mathbf{L}\psi^{(i)} = \mathbf{S}\psi^{(i-1)}, \quad i > 0 \tag{5.8}$$

Here the uncollided flux has general boundary conditions per Eq. 2.4 since all incident neutrons from outside the system are considered uncollided in the system. As such, all collided equations are given vacuum boundary conditions so that $\Gamma\left(E, \vec{\Omega}, t\right) = 0$ per Eq. 2.4. A Monte Carlo simulator is then used to estimate $\psi^{(i)}$ for a given number of collisions $i = 0, \ldots, n-1$, which can be combined into the $n-1$ collided flux, ψ_{MC}, estimated by the Monte Carlo simulator,

$$\psi_{MC} = \sum_{i=0}^{n-1} \psi^{(i)} \tag{5.9}$$

Now the distributed source of particles that have undergone exactly n collisions for the S_N calculation can be expressed as,

$$\mathbf{Q}_n = \mathbf{S}\psi^{(n-1)} \tag{5.10}$$

This source then "drives" a transport problem for flux with n or more collisions whose solution will now be referred to as ψ_{n+}. Using linear superposition this flux can be rewritten in the form,

$$\psi_{n+} = \sum_{i=n}^{\infty} \psi^{(i)} \tag{5.11}$$

The transport equation in Eq 5.5 can then be rewritten as,

$$\mathbf{L}\psi_{n+} = \mathbf{S}\psi_{n+} + \mathbf{Q}_n \tag{5.12}$$

This equation can be used to calculate the remaining collision-count fluxes, ψ_{n+}, using an S_N solver, THOR in our case, yielding the flux for n or more collisions, thus providing ψ_{n+}. Equations 5.6, 5.9, and 5.11 can be combined to obtain,

$$\psi = \sum_{i=0}^{\infty} \psi^{(i)} = \sum_{i=0}^{n-1} \psi^{(i)} + \sum_{i=n}^{\infty} \psi^{(i)} = \psi_{MC} + \psi_{n+} \tag{5.13}$$

Given both a n[th] collided source and the flux sum of $(n-1)$ or fewer collisions from a Monte Carlo simulator, a deterministic code can evaluate the remaining collided fluxes, and these can be combined into the total flux that satisfies the original problem. To further confirm the correctness of this formalism, these fluxes in Eq. 5.13 can be substituted into Eq 5.5 to get,

$$\mathbf{L}(\psi_{MC} + \psi_{n+}) = \mathbf{S}(\psi_{MC} + \psi_{n+}) + \mathbf{Q} \tag{5.14}$$

Now Eq 5.12 is substituted into Eq. 5.14 to obtain,

$$\mathbf{L}\psi_{MC} + \mathbf{S}\psi_{n+} + \mathbf{Q}_n = \mathbf{S}\psi_{MC} + \mathbf{S}\psi_{n+} + \mathbf{Q} \tag{5.15}$$

Plugging in Eq 5.9 and simplifying this becomes,

$$\mathbf{L}\psi^{(0)} + \sum_{i=1}^{n-1} \mathbf{L}\psi^{(i)} + \mathbf{Q}_n = \sum_{i=0}^{n-2} \mathbf{S}\psi^{(i)} + \mathbf{S}\psi^{(n-1)} + \mathbf{Q} \tag{5.16}$$

Looking back at Eqs. 5.10 and 5.7, terms cancel to get,

$$\sum_{i=1}^{n-1} \mathbf{L}\psi^{(i)} = \sum_{i=0}^{n-2} \mathbf{S}\psi^{(i)} \tag{5.17}$$

Comparing to Eq 5.8 it can be seen that this is indeed consistent and correct thus verifying our proposed coupling formalism.

This shows that in theory Monte Carlo simulations can solve for low-count collided flux values and pass them on to S_N solvers to get the full distribution of the flux over phase space. The Monte Carlo flux clearly does not suffer ray effects, and under certain conditions the S_N flux will have mitigated ray effects thereby improving the quality of the combined flux solution.

Currently, isotropic scattering is assumed, and the Monte Carlo calculation only provides the scalar flux, which is the directionally integrated angular flux. This is used to evaluate the scattering source that drives the S_N calculation. This assumption could be relaxed in both THOR

and Hammer to allow for scattering anisotropy, requiring spherical harmonic moments of the angular flux and the scattering sources to be tallied in the Monte Carlo simulation.

5.5.2 Practical Hammer-THOR Coupling Method

Calculation of the n^{th} collided source from the $(n-1)$ collided flux was implemented in the auxiliary code. This flux was provided by the Monte Carlo code Hammer, along with total flux of neutrons that are uncollided to experienced $(n-1)$ collisions. This output is parsed using a coupling software that transforms it into a source format that is compatible with THOR. This method involves multiplying the low-count collided flux in each tetrahedral cell by the scattering and fission cross sections in that cell, group by group, in order to create the new energy-dependent, distributed external source, per Eq 5.10. The software additionally alters the mesh file to be able to properly use this source. Because THOR separates source values by source region this method requires every single cell to be a separate source region. The new external source is mapped in order of cells so that cell 1 is assigned new source 1. The method is currently limited to isotropic scattering cross sections and scalar flux data from Hammer, though the coupling equations are general and can be expanded to include any order of collision for angular flux with anisotropic scattering. It should be noted though, that since the output of Hammer is currently limited to the scalar flux, anisotropic scattering cross section application will not alter the produced n^{th} collided flux.

Once the S_N calculation is completed, the solution is added to the sum of all collision counts flux from the Monte Carlo simulation to give the total flux solution per Eq 5.13. This is done specifically with the scalar flux since our primary objective is to compute detector response. The resulting total flux can now be used to calculate a detector response or plotted to visualize the coupled solution over the spatial domain.

5.6 BeRP Ball in a Box Model

With the capabilities of THOR expanded to include the general collision-count coupling with Hammer, a model was created that allows visual observation of ray effects in a 3D test problem for THOR as well as their subsequent mitigation through the coupled method described in Section 5.5. This model involved the bare BeRP ball located at the center of a cube of air, that is approximated here with vacuum. This cube of air was made to be 203.2 cm wide, or 80 in, a little less than 10 times the diameter of the ball plus the largest reflector. An illustration of the model as rendered by SolidWorks is shown below in Fig. 5.5.

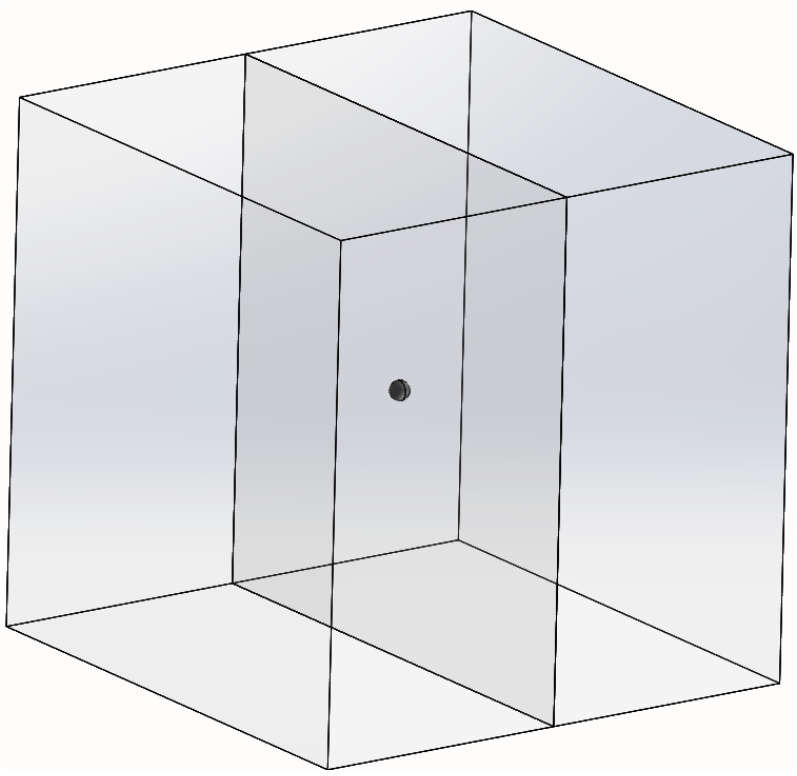

Figure 5.5: BeRP ball in cube of air rendered by SolidWorks.

It can be seen that the cube of air is far larger than the plutonium sphere. Since the air is a low collision medium and the plutonium sphere is a very localized source, it is expected that a discrete ordinates calculation will suffer from severe ray effects at the bounding faces of the air

cube. The correct flux profile for the box can be approximated as a point source in a vacuum far from the sphere. The scalar flux solution of such a problem can be written as,

$$\phi = \frac{C}{(x-x_0)^2 + (y-y_0)^2 + (z-z_0)^2} \tag{5.18}$$

where (x_0, y_0, z_0) is the location of the point source and C is some constant that scales linearly with the source strength. Setting the location of the point source at the center of the sphere and C=1 will provide an approximation of the expected shape of the flux for this problem and will allow a comparison baseline to measure the adverse influence of ray effects against. However, it is noted that this approximation should not be confused for the true solution as the actual problem contains a distributed, even if highly localized, external source. Also, while air has very low cross sections due to its density, it is not a true vacuum. Finally, the actual computed solution will involve a constant, i.e. averaged, scalar flux in each cell inconsistent with the analytic solution, Eq. 5.18, that provides an exact value for every single point (x, y, z).

5.6.1 Multigroup Cross Sections Generated by SERPENT

Two group Cross sections for this problem were generated by running the SERPENT Monte Carlo code for a configuration identical to the one described above and shown in Fig 5.5. The energy cutoff for the cross sections was 0.625eV. The cross sections were validated by running them in eigenvalue mode with THOR. The THOR calculated eigenvalue using a S_8 quadrature set was 0.802577 compared to the k_{eff} calculated by SERPENT of 0.773667. The fact that the system is evaluated on a tetrahedral mesh adds spatial error in the eigenvalue solution since the spherical BeRP ball cannot be resolved exactly by a tetrahedral mesh. As our ultimate target application is a detector problem not a reactor simulation the importance of eigenvalue is diminished. This 3% error in the eigenvalue for this external source problem confirms that our SERPENT-generated cross sections are sufficiently accurate for use in THOR and more

importantly yield a subcritical assembly, a necessary condition for the existence of a steady state solution to external source problems with multiplication as mentioned in Section 5.1.

5.6.2 THOR Mesh

A THOR compatible mesh was generated in SolidWorks from the configuration described above and shown in Fig. 5.5. The mesh featured 6,101 vertices and 34,537 tetrahedra. The mesh was made finer in the BeRP ball, i.e. generally short edges of the tetrahedral, and gradually became coarser with increasing distance from the sphere's center to form the air cube. This resulted in the BeRP Ball being modeled by 1,976 cells with an average cell volume of 0.112378146 cm^3 resulting in a sphere total modeled volume of 222.06cm^3 which is about 2.9% smaller than the true sphere's volume of 228.72cm^3. The air took up the remaining 32,561 cells with an average cell volume of 258 cm^3 for a total volume of 8,389,956cm^3 which is almost exactly the same as the computed volume of 8,389,948cm^3. The error in the BeRP Ball volume adversely affects the magnitude of the solution, however because the sole purpose of this model is to visually inspect the flux profile for evidence of ray effects and their mitigation, the flux magnitude discrepancy is not central to this investigation.

5.6.3 Hammer Model

Using the mesh conversion tool THOR Mesh Generator, the CSG model described above and shown in Fig 5.5 was transformed into a format compatible with Hammer. The model was further completed by the addition of multigroup cross sections to be used by the code that were likewise converted by the cross-section format converter code THORxsGen described in Section 5.3.1. The model was created to permit execution for an arbitrary number of collisions to be coupled with THOR. Additional variance reduction was performed by the Hammer development team at the University of Michigan to allow for better flux accumulation in regions with low

collision counts as is the case in the air cells. The THOR mesh was used by the Hammer code to tally flux for the cells in order to be enable the coupling of the results as described in Section 5.5.2.

5.7 BeRP with SNAP Model

To demonstrate the detrimental influence of ray effects on detector problems another configuration was created to model a simplified version of the experiment performed at the DAF described in Chapter 2. This configuration has been previously described in Section 4.2 and is illustrated in Fig. 4.5. The reference values of the detector response for this model as computed by MCNP using the simplified model are given in Table 4.3. This model was created for both the case with the HDPE shield in front of the SNAP and the case without the shield.

5.7.1 Multigroup Cross Sections Generated by SERPENT

Two group Cross sections for this problem were generated by running the SERPENT Monte Carlo code for a system identical to the one described in Section 4.2 and shown in Fig 4.5. The energy cutoff for the cross sections was 0.625eV. In total seven materials were modeled and given cross sections for the problem.

5.7.1.1 Simulation with Multigroup MCNP

The cross sections generated for this model have two major inherent errors associated with them. First, the collapse from continuous energy to multigroup introduces errors due to the varying spectrum of the flux. The goal is to have reaction rates preserved as expressed in Eq. 2.2. To this end the average flux spectra in a material is considered when collapsing cross sections to best preserve the reaction rates. However, some regions may have a flux spectrum that looks very different from other regions of the same material. This will lead to error in both regions since the average will differ from both. A homogeneous problem with a uniform flux spectrum

does not suffer this issue, however with this problem there are a few locations where the spectrum changes drastically. The spectra further in the polyethylene sections in the problem is likely to be more thermal than the spectrum on the outside of these sections, yet they will both be attributed the same multigroup cross section. There are a few ways to mitigate this error. The most common method involves increasing the number of energy groups. Finer group structures lend to a lower probability that a group exists at two very different energy distributions (and consequently different correct cross sections) in a given problem. Another method involves separating out sections of a material into different regions for different cross section sets. This allows for the spectrum to be more accurately captured spatially since not all instances of a given material are given the same cross section data.

The second major error associated with these multigroup cross sections is the assumption of isotropic scattering. Physical particle scattering is anisotropic to varying degrees in nature. This anisotropy is captured in multigroup cross sections through angular moments to give a more realistic view of the scattering mechanism. However, this does complicate the calculation of the secondary source since it can no longer be computed with the scalar flux alone. For this reason, the cross sections in this work will be restricted to isotropic scattering and the application of the method in Section 5.5 is only implemented for isotropic scattering. Nevertheless, the formalism is general and can be applied to anisotropic scattering to enhance accuracy of the calculation.

With these two errors in mind, analysis was performed on the accuracy of the cross sections for the simplified SNAP model. The simplified model was simulated with MCNP using the multigroup cross sections generated by SERPENT. The results were recorded and compared to the results from the simplified model continuous-energy MCNP runs and shown in Table 5.1.

Table 5.1: Multigroup MCNP *vs* Continuous-energy MCNP comparison

Case	MCNP	Uncertainty	MCNP MG	Uncertainty	ARE
Poly Shield	33.534	3.30%	22.0131	3.89%	34.36%
No Poly Shield	41.883	3.07%	50.0725	2.56%	19.55%

This shows that the introduction of the two group cross sections with isotropic scattering represents a large error in the count rate that far exceeds the simulation's statistical uncertainty. With relative error versus the continuous energy simulation ranging of 19.55% and 34.36%, the error is substantial compared to the continuous-energy simplified run in MCNP. Because of this discrepancy, comparisons between THOR and coupled Hammer-THOR results will be made against the multigroup MCNP solutions as they represent the true goal count rates for the multigroup models calculated with either pure discrete ordinates or coupled S_N and MC. This comprises a *numerical validation* since the underlying methods and codes are all numerical but are substantively different in methodology and implementation.

5.7.2 THOR Mesh

A THOR compatible mesh was generated in SolidWorks from the configuration described in Section 4.2 and shown in Fig 4.5. Two versions of the problem were meshed, one with the HDPE shield attached to the SNAP detector and one without. The mesh without the SNAP shield featured 18,278 vertices and 105,166 tetrahedra. A summary description of the mesh including region-volume absolute relative error is shown in Table 5.2.

Table 5.2: Simplified Model Meshing Information without the HDPE SNAP Shield.

Region	1	2	3	4	5	6	7	All
Material	Poly	Dead Helium	Active Helium	"Heavy" Poly	Cadmium	Air	Plutonium	Total
Modeled Volume [cm^3]	6.15245E+03	3.83814E+01	4.54890E+01	6.78477E+02	1.39262E+02	6.67361E+05	2.28724E+02	6.74644E+05
Meshed Volume [cm^3]	5.78687E+03	3.59545E+01	4.16401E+01	6.83153E+02	1.39376E+02	6.67729E+05	2.27511E+02	6.74644E+05
Number of Cells	13217	199	263	25472	21316	26640	18059	105166
Average Cell Size [cm^3]	4.37835E-01	1.80676E-01	1.58327E-01	2.68197E-02	6.53857E-03	2.50649E+01	1.25982E-02	6.41504E+00
ARE	5.94204%	6.32295%	8.46132%	0.68916%	0.08185%	0.05518%	0.53019%	0.00000%

The data shows that the error in the plutonium volume is very small, similarly the cadmium sleeve and the inner polyethylene sleeve (“Heavy” poly). Error present in the volume of the rest of the polyethylene as well as the helium may make a non-negligible difference in the results though. The total flux in the active helium is the determining factor in the count rate calculated for the system, therefore an error in active helium volume will have a direct impact on the computed response. The mesh with the SNAP shield was made more refined and featured 34,280 vertices and 202,950 tetrahedra. A summary description of the mesh including region-volume absolute relative error is shown in Table 5.3.

Table 5.3: Simplified Model Meshing Information with the HDPE SNAP Shield

Region	1	2	3	4	5	6	7	All
Material	Poly	Dead Helium	Active Helium	"Heavy" Poly	Cadmium	Air	Plutonium	Total
Modeled Volume [cm^3]	7.21480E+03	3.83814E+01	4.54890E+01	6.78477E+02	1.39262E+02	6.66299E+05	2.28724E+02	6.74644E+05
Meshed Volume [cm^3]	7.09216E+03	3.77185E+01	4.45788E+01	6.78425E+02	1.39402E+02	6.66424E+05	2.27511E+02	6.74644E+05
Number of Cells	30592	3561	5322	82714	21421	41476	17864	202950
Average Cell Size [cm^3]	2.31831E-01	1.05921E-02	8.37632E-03	8.20206E-03	6.50771E-03	1.60677E+01	1.27357E-02	3.32419E+00
ARE of Volume	1.69984%	1.72694%	2.00100%	0.00758%	0.10028%	0.01881%	0.53018%	0.00000%

The data shows that the error in the plutonium volume is very small, similarly the cadmium sleeve and the inner polyethylene sleeve (“Heavy” poly). Error present in the volume of the rest of the polyethylene as well as the helium has been reduced compared to the mesh for the problem without the HDPE shield described in Table 5.2. However, the error present in the polyethylene and helium regions is still over 1% and will likely have a noticeable impact on the results.

Adaptive meshing was implemented to allow for a mesh that was more refined in regions where the geometry description is difficult to express with a coarser mesh. An example of this is shown in Fig 5.6.

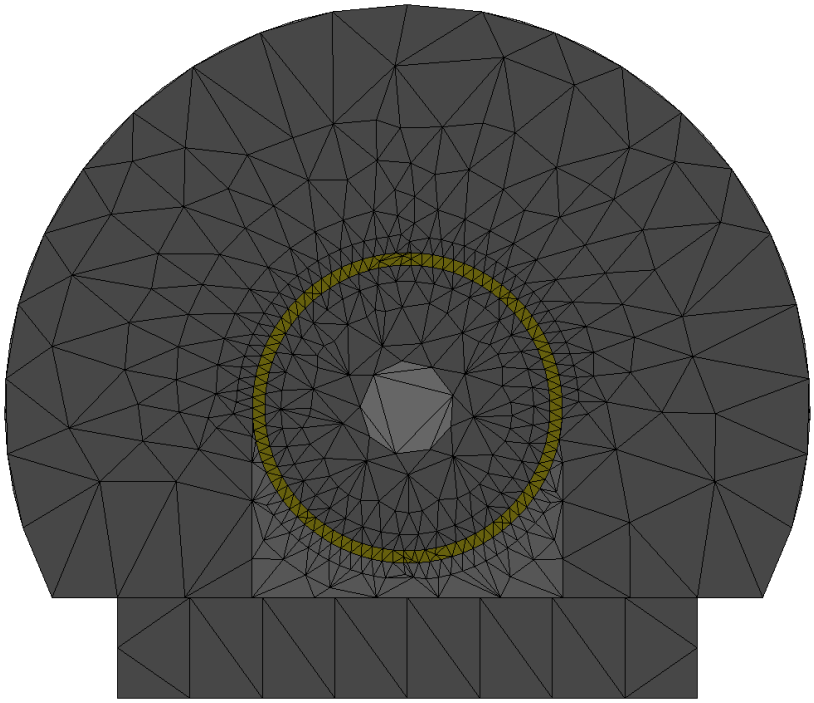

Figure 5.6: Adaptive Mesh of the SNAP Detector.

It can be seen that the thin cadmium region (here in gold) is refined much more finely than the regions of polyethylene, and the change in refinement happens gradually moving away from the edge of the cadmium. This allows for accurate geometric descriptions of small parts of the model as quantified by the volume errors in Tables 5.2 and 5.3.

5.7.3 Hammer Model

Using the conversion tool THOR Mesh Generator, the CSG model described in Section 4.2 and shown in Fig. 4.5 was transformed into a format compatible with Hammer. The model was further completed by the addition of multigroup cross sections to be used by the code that were likewise converted by the format converter THORxsGen described in section 5.3.1. The model enables Hammer execution with an arbitrary number of collisions and the resulting external source is coupled with THOR. The detector response is dominated by neutrons that arrive straight at the detector from the source rather than being scattered into the detector by the

intervening air. Since the detector is structurally composed of HDPE, which has a large downscattering cross section, the special variance techniques to get tallies in air are unnecessary for this problem. The THOR mesh was used by the Hammer code to tally the two-group flux in all cells in order to enable the coupling for this system as described in Section 5.5.2.

Chapter 6. Computation Results and Numerical Validation

In order to compare the effectiveness of the coupling method in mitigating ray effects, two computational experiments were performed. The first set of experiments presented in Section 6.1 involved the BeRP Ball in the air cube described in Section 5.6 to show visual reduction of ray effects when THOR is coupled to Hammer. The second set of experiments presented in Section 6.2 involved the simplified SNAP experiment model described in Sections 4.2 and 5.7 to demonstrate the practical use in mitigating ray effects. The latter also serves the numerical validation objective of this Thesis. These systems were solved in two different manners. First each problem was solved using pure discrete ordinates method with THOR employing varying quadrature orders. Second, they were solved using the coupled Hammer-THOR method described in Section 5.5 with varying collision-counts in the Monte Carlo stage computed by Hammer and varying quadrature orders in THOR.

6.1 BeRP Ball in Air Test Problem: Mitigation of Ray Effects

Results for the system described in Section 5.6 are inspected visually for the presence of ray effects, specifically on the domain outer face of the air cube. Comparison of flux profile is made against the solution of Eq. 5.18 projected on THOR's mesh triangular faces on the subject face as shown in Fig 6.1.

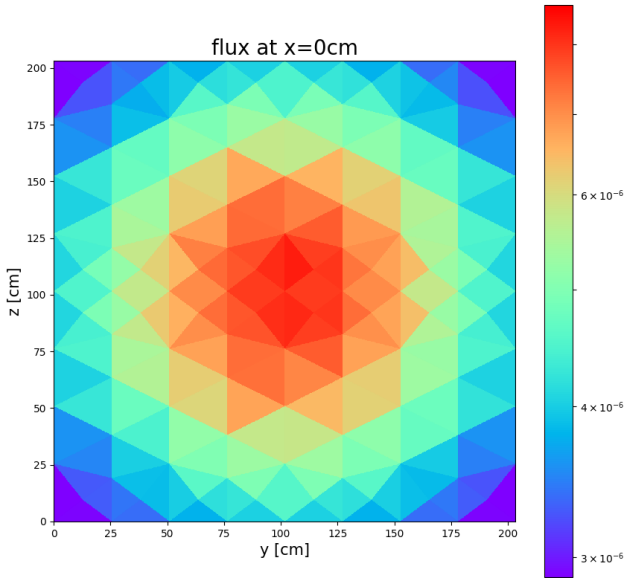

Figure 6.1: Flux Due to a Point Source in a Vacuum at Cube's Outer face.

It must be reiterated though that this is not the actual solution, but rather an approximation of the expected shape on the problem mesh. Each triangle is assigned a uniform value equal to the flux associated with its geometric center point per Eq. 5.18. See Section 5.6 for further details.

The computational results shown in the subsequent sections are for fast flux in the two-group problem. Subcritical induced fission is turned off here as it is not necessary for demonstrating visible ray effects.

6.1.1 Varying Quadrature Order in Pure S_N Calculation

The system was tested with pure S_N calculations, THOR, for 4 different quadrature orders of discrete ordinates. These results are depicted over the left outer face of the cube domain, or 101.6cm away from the localized plutonium source at the center of the domain which was given a source strength of 1 n/(s cm^3). The resulting flux profile for the S_2 (1 angular direction per octant) calculation is shown in Fig 6.2.

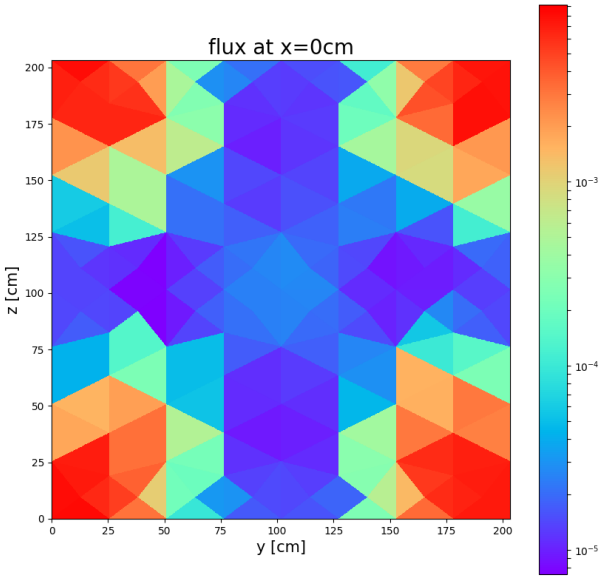

Figure 6.2: Flux at Cube's Outer Face Due to BeRP Ball in Air with S_2 Quadrature.

Ray effects can be clearly seen as the flux peaks are relegated to the corners of the domain where the quadrature angles can be traced directly back to the BeRP ball isolated source. Clearly the peak flux for this configuration, see Fig. 6.1, should reside at the center of the depicted face where the distance to the localized source is shortest, hence the geometric attenuation is smallest. The erroneous flux profile shown in Fig. 6.2 will cause a detector placed at the center of the considered domain outer face to have a very low chance of detecting a representative flux magnitude and a correspondingly accurate count rate. Results for the S_4 (3 angular directions per octant) calculation are shown in Fig 6.3.

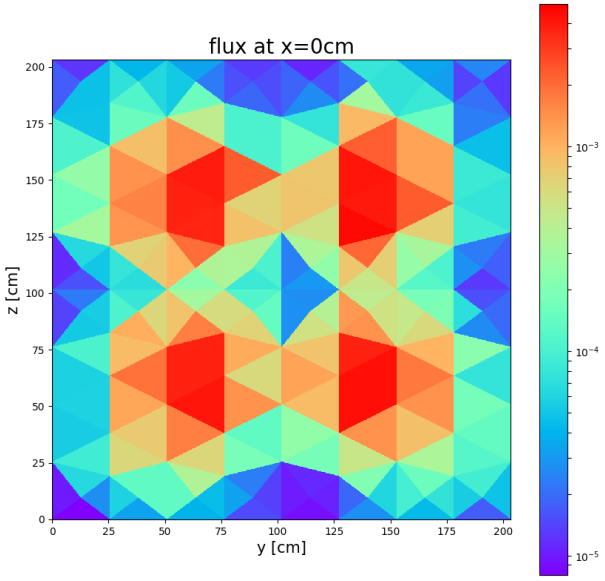

Figure 6.3: Flux at Cube's Outer Face Due to BeRP Ball in Air with S_4 Quadrature.

Ray effects are still visibly present in this case too, though they are less separated now, i.e. the flux peaks pull closer to their true location at the center. This improvement is a result of the S_4 quadrature set containing angles that are closer together. At a further distance from the source, though, the ray effects would look similar to the S_2 case, i.e. peaks shifting farther from the center. Results for the S_8 (10 angular directions per octant) calculation are shown in Fig 6.4.

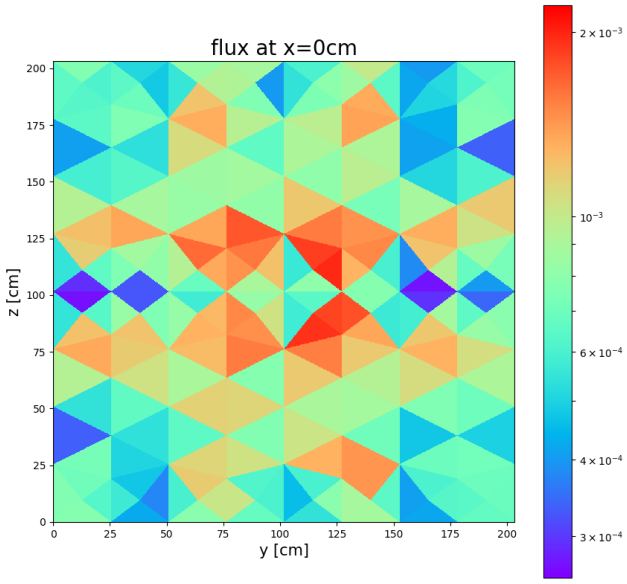

Figure 6.4: Flux at Cube's Outer Face Due to BeRP Ball in Air with S_8 Quadrature.

Ray effects here are quite visible as nonphysical gaps are present in many of the cells along the major axes of the domain, namely the center of the plotted square. Because angular quadratures shy away from angles close to parallel to the axes, this is the location one would expect gaps in the flux profile to be visible even in high order quadrature calculations. The highest order quadrature solutions for this model were obtained with S_{16} (36 angular directions per octant) calculations and are shown in Fig 6.5.

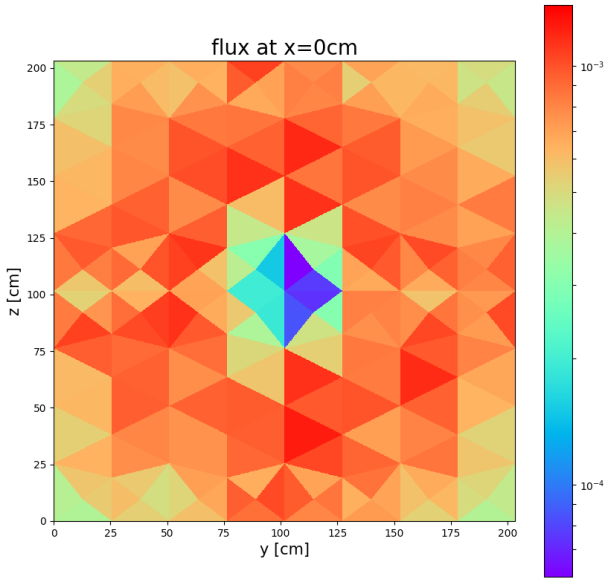

Figure 6.5: Flux at Cube's Outer Face Due to BeRP Ball in Air with S_{16} Quadrature.

Fig 6.5 shows a flux profile that in some locations resembles the true shape demonstrated in Fig. 6.1. However, ray effects are severe enough to leave a gap in the flux profile at the center of the face. This shows that even with the computationally expensive S_{16} calculation (which solves the discrete ordinates equations along a total of 288 angular directions in the 3D domain), ray effects are still detrimental to accuracy at the outer face of this problem domain. This demonstrates that increasing angular quadrature order may not always suitably mitigate ray effects.

6.1.2 MC and S_N Coupling

Applying our new method described in Section 5.5, this same problem was also solved by the coupled Monte Carlo code Hammer with the discrete ordinates code THOR. Since the goal of the method is to be effective in the mitigation of ray effects even for low order S_N calculations, all results shown here are obtained with the S_2 discrete ordinates quadrature. For this reason, these results should be primarily compared for visible ray effects against Fig. 6.2. The collision-count in Hammer is varied to demonstrate the effectiveness of the method with increasing count of the collided flux. This is important because the traditional method detailed in Section 2.2.6 only used the uncollided flux and first collision source to mitigate ray effects, whereas our method allows for a more general collision-count coupling. These results are also executed with fission disabled for a more direct comparison to the results in the previous section and the results shown below are similarly for the fast neutron group only.

It should also be noted that the units of these results are not consistent compared to results in the previous section. That is to say, due to flux normalization in the Monte Carlo solutions, magnitudes of the flux in this section will differ compared to the flux in the previous section. For this reason, results in this section and the section before should be interpreted with emphasis on the flux shape and relative changes in flux magnitude for a single run without regard to changes in magnitude between calculations.

Results from the S_2 calculation coupled with uncollided flux (1^{st} collision source) are shown in Fig 6.6.

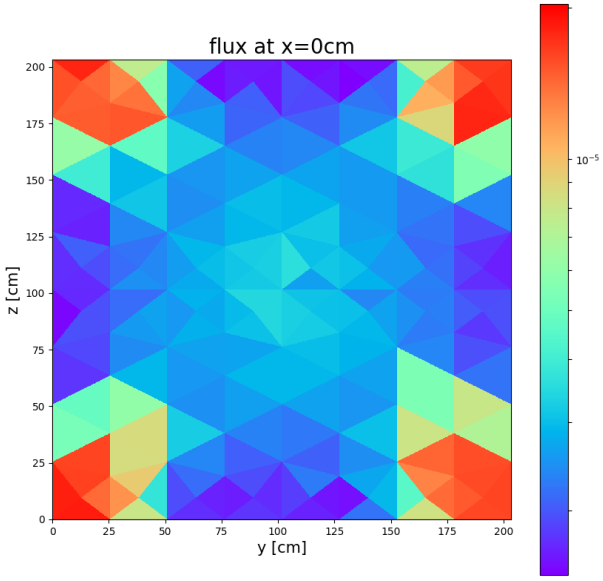

Figure 6.6: S_2 Coupled with MC Uncollided Flux at Cube's Outer Face Due to BeRP Ball in Air.

This plot shows that the ray effects are still visible but comparison to Fig 6.2 shows that there is at least some additional distribution of the flux near the center of the face. It is then evident that higher collision-count flux from Monte Carlo is necessary in some problems, making the 1st collision source sometimes ineffective. Results from the S_2 calculation coupled with first collided flux (2nd collision source) are shown in Fig 6.7.

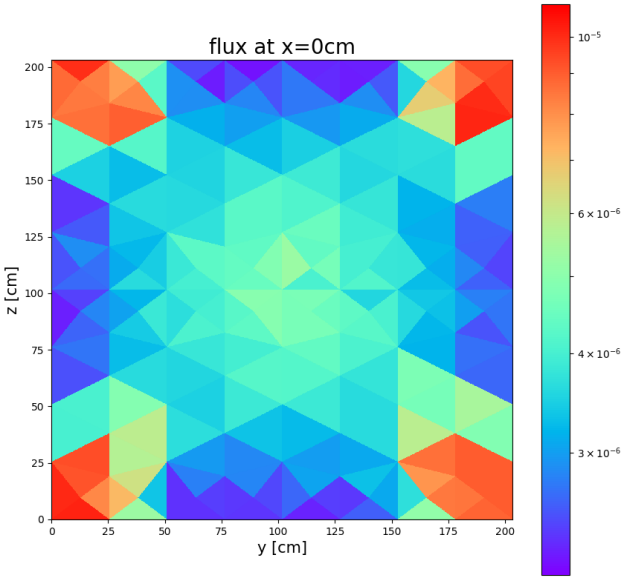

Figure 6.7: S_2 Coupled with MC First Collided Flux at Cube's Outer Face Due to BeRP Ball in Air.

Once again, the ray effects are still visible at the face's corners, but a clear increase in the flux distribution near the center of the slice is evident. Hence, we note that success in mitigating ray effects improves as the collision-count of the Monte Carlo simulation increases. Results from the S_2 calculation coupled with second collided flux (3^{rd} collision source) are shown in Fig 6.8.

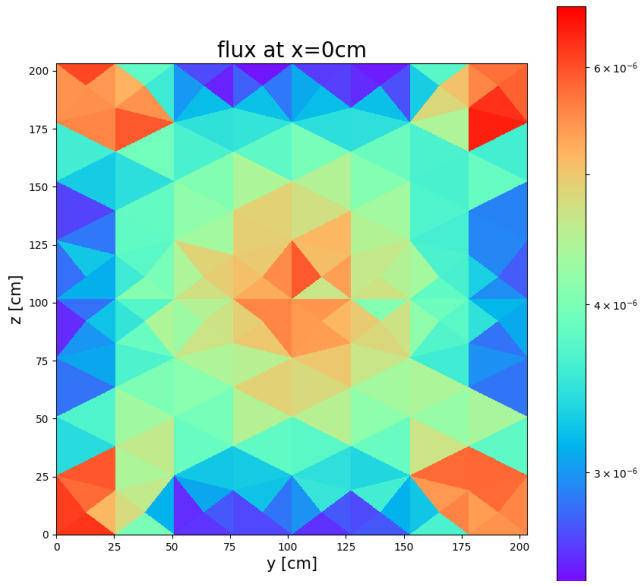

Figure 6.8: S_2 Coupled with MC Second Collided Flux at Cube's Outer Face Due to BeRP Ball in Air.

At this point, while the ray effects are still prominent at the four corners, the flux near the center of the slice is of comparable magnitude to the unphysically high flux along the rays from the localized source. Results from the S_2 calculation coupled with third collided flux (4^{th} collision source) are shown in Fig 6.9.

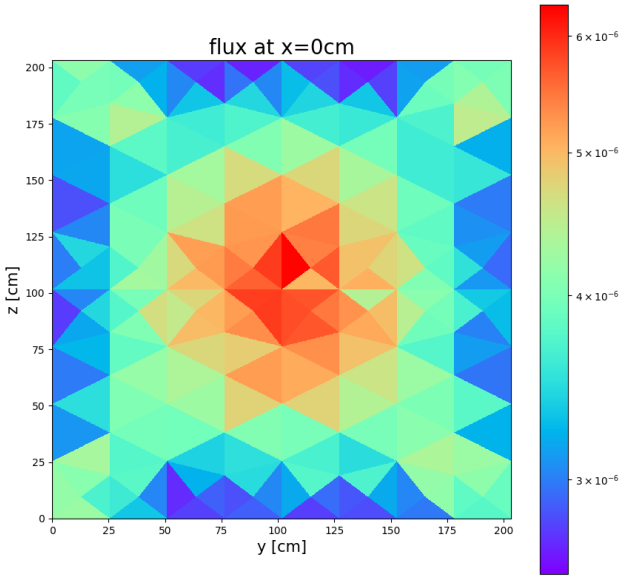

Figure 6.9: S_2 Coupled with MC Third Collided Flux at Cube's Outer Face Due to BeRP Ball in Air.

While ray effects are still visibly present in this calculation, it is clear that the magnitudes of the ray effects are now substantially less than the flux in the center of the slice where the flux's true peak resides. The flux now closely resembles the approximate expected shape of Fig 6.1 with the primary difference being the mitigated ray effects at the corners of the slice. Indeed, it seems that ray effects are less visible in this solution than in the S_{16} calculation observed in Fig 6.5. Results from the S_2 calculation coupled with fourth collided flux (5^{th} collision source) are shown in Fig 6.10.

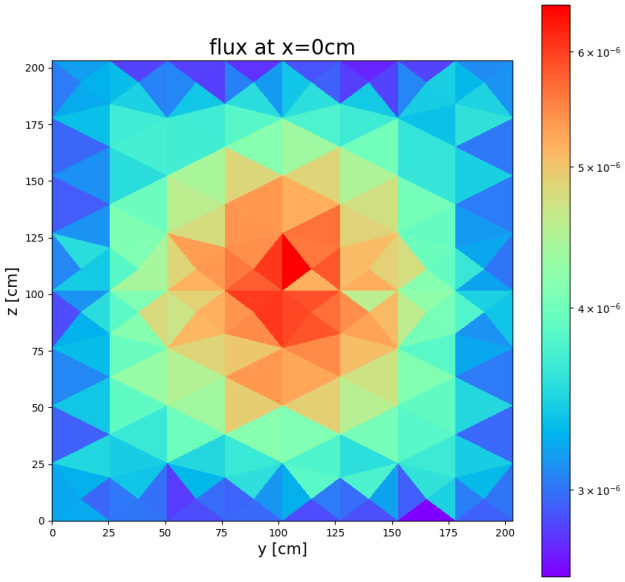

Figure 6.10: S_2 Coupled with MC Fourth Collided Flux at Cube's Outer Face Due to BeRP Ball in Air.

For this calculation the ray effects are almost invisible. The flux shape closely resembles that of Fig 6.1 and the corners no longer seem to possess the flux peaks characteristic of ray effects in discrete ordinates calculations. Comparing to Figs. 6.2 through 6.5 we observe that for this configuration coupling Hammer's fourth collided flux with a S_2 quadrature in THOR mitigates visible ray effects better than increasing the quadrature order even up to S_{16}.

6.2 BeRP Ball with SNAP Detector: Numerical Validation

Results for the system described in Sections 4.2 and 5.7 are considered for the practical reduction of ray effects in a measurable quantity, specifically the predicted count rate in the SNAP detector. This count rate is calculated by spatially integrating the computed scalar flux in all cells in the active helium and then multiplying each group's total flux by the (n,p) reaction cross section for that group in Helium-3. This provides a value of the count rate that is comparable to the multigroup MCNP results presented in Table 5.1 to establish numerical validity of the coupled THOR-Hammer model. Full validation of this model requires reducing

the errors from other model simplifications, primarily the number of groups employed. The purpose of the work presented in this section is to establish the principle that coupled MC-S_N is effective in reducing adverse ray effects on detector count rates relative to a simplified comparable-physics model. Future work will address a full-fledged validation via numerical validation against continuous-energy MC and experimental validation against measured count rates. However, even for the preliminary numerical validation reported here, it must be remembered that there is additional meshing error associated with the mesh created for THOR so the obtained count rates suffer this additional discretization error.

6.2.1 Varying Quadrature Order in Pure S_N Calculation

The configuration was tested with pure S_N calculations for 4 different quadrature orders of the discrete ordinates approximation. These results are calculated with fission turned on in the BeRP ball. Results for all pure discrete ordinates calculations for the case without the HDPE shield in front of the SNAP are shown in Table 6.1.

Table 6.1: S_N Count Rates for the BeRP Ball and SNAP without the HDPE Shield and ARE Relative to the Multigroup MCNP Value in Table 5.1.

N	Count Rate [1/s]	ARE
2	0.0038025	99.99%
4	0.18830	99.62%
8	7.1251	85.77%
16	61.533	22.89%

These results are contrasted to the multigroup MCNP results presented in Table 5.1 which showed a count rate of 50.073/s and the ARE for each quadrature order is so indicated. It must be stressed though that this reference count rate does not consider errors introduced by the meshing of the geometry. However, it is still clear from these results that a more reasonable count rate can be achieved through the increase in the order of the discrete ordinates quadrature.

Results for all pure discrete ordinates calculations for the case with the HDPE shield in front of the SNAP are shown in Table 6.2.

Table 6.2: S_N Count Rates for the BeRP Ball and SNAP with the HDPE Shield and ARE Relative to the Multigroup MCNP Value in Table 5.1.

N	Count Rate [1/s]	ARE
2	0.0031133	99.99%
4	0.10344	99.53%
8	4.1426	81.18%
16	33.425	51.84%

These results have their relative error calculated against the multigroup MCNP results presented in Table 5.1 which showed a count rate of 22.013/s. These results show that the count rate becomes closer to the MCNP reference value as the order of the discrete ordinates quadrature increases. It can be seen though with both cases in Tables 6.1 and 6.2 that even with S_{16} calculations the results still show large errors. This should not be surprising as even with S_{16} calculation, the better results are largely due to cancelation of errors, if the right number of rays hit and miss the detector, then the integral result could happen to be better while still locally experiencing severe ray effects. This correct ratio of rays hitting and missing the detector is more likely to happen as more angles are added in a higher-order angular quadrature. However, the ray effects are still present and negatively impact the accuracy of the count rates. This is expected when considering the flux profile in Fig. 6.5 which show the flux distributed over a plane that is about the same distance from the BeRP ball as the detector's front face in the present test configuration. The gap in the flux profile noted earlier in Fig. 6.5 at the center of the considered face overlaps with the detector location and adversely affects the accuracy of the count rate as evident from the AREs in excess of 50% appearing in Table 6.2.

6.2.2 MC and S_N Coupling

Applying our new method described in Section 4.5, this same problem was also solved by coupling the Monte Carlo code Hammer with the discrete ordinates code THOR. Since the goal of the method is to mitigate ray effects even for low order S_N calculations, all results shown here are the result of the coupling performed with S_2 discrete ordinates equations unless otherwise noted. For this reason, these results should be compared to the results in Tables 6.1 and 6.2 with reference to the Multigroup MCNP values reported in Table 5.1. The collision-count in Hammer is varied to demonstrate the effectiveness of the method at different levels of collided flux. These results are obtained with fission disabled except the first case which is also run with fission enabled in order to compare the effectiveness of the method for the localization level of the secondary source (since fission creates a more localized secondary source). The cases run with fission disabled are multiplied by correction factors for each energy group that were determined through numerical experiments in MCNP to account for the effect of enabling fission on the flux in the active helium region.

Coupled MC-S_N count rates for the first system with fission enabled are shown in Table 6.3 together with AREs relative to the reference value reported in Table 5.1.

Table 6.3: Coupled Hammer-THOR Results for the BeRP Ball and SNAP without the HDPE Shield and Fission Enabled.

N	Collision Order	Count Rate [1/s]	ARE
2	0	4.5293	90.95%
2	1	7.5885	84.84%
2	2	11.234	77.56%
2	3	13.580	72.88%
2	4	16.226	67.59%
2	5	18.377	63.30%
2	6	20.444	59.17%
16	6	51.828	3.51%

Table 6.3 shows significant improvement over the S_2 values listed in Table 6.1 even when just coupling with the uncollided flux. The improvement does seem to slow down as the collision order increases. For this calculation the secondary source is still very localized due to the enabling of fission multiplication in the BeRP Ball. For this reason, the calculation was also performed with fission disabled applying the correction factors described above. Coupled results for the first system with fission disabled are shown in Table 6.4.

Table 6.4: Coupled Hammer-THOR Results for the BeRP Ball and SNAP without the HDPE Shield and Fission Disabled.

N	Collision Order	Count Rate [1/s]	ARE
2	0	30.863	38.36%
2	1	40.324	19.47%
2	2	46.875	6.39%
2	3	49.360	1.42%
2	4	50.502	0.86%
2	5	51.191	2.23%
2	6	51.935	3.72%
16	6	51.125	2.10%

Here the results are much improved approaching the reference value much faster with increasing collision-count in the Hammer calculation, leveling off rapidly as the collision-count increases. The S_{16} calculation coupled with the 6^{th} collided flux produces a count rate that is almost the same value as computed with the 4^{th}, 5^{th}, and 6^{th} collided S_2 calculations.

The fact that the count rate has leveled off with increasing collision-count suggests that ray effects have mostly been eradicated. From this observation, since Table 5.1 does not account for errors incurred in meshing the problem, it is conjectured that the reference result for this problem once meshed is likely closer to the S_{16} calculation coupled with 6^{th} collided flux. This is reasoned from the diminishing effect of higher collision-count calculations. So, the solution with

a high order discrete ordinates calculation coupled with high collision-count Monte Carlo results should yield an accurate solution (though they are both close as seen from their ARE values).

S_2 is a less common than some other S_N calculations due to its low order nature. While it is ideal for demonstrating ray effects and their mitigation, since ray effects are most severe in lower order calculations, a better representation of a typical discrete ordinates calculation would be obtained with the S_8 equations. For this reason, the coupled calculation is also performed using S_8 without fission.

Results of coupling solutions from Table 6.3 and 6.4 are plotted in Fig 6.11.

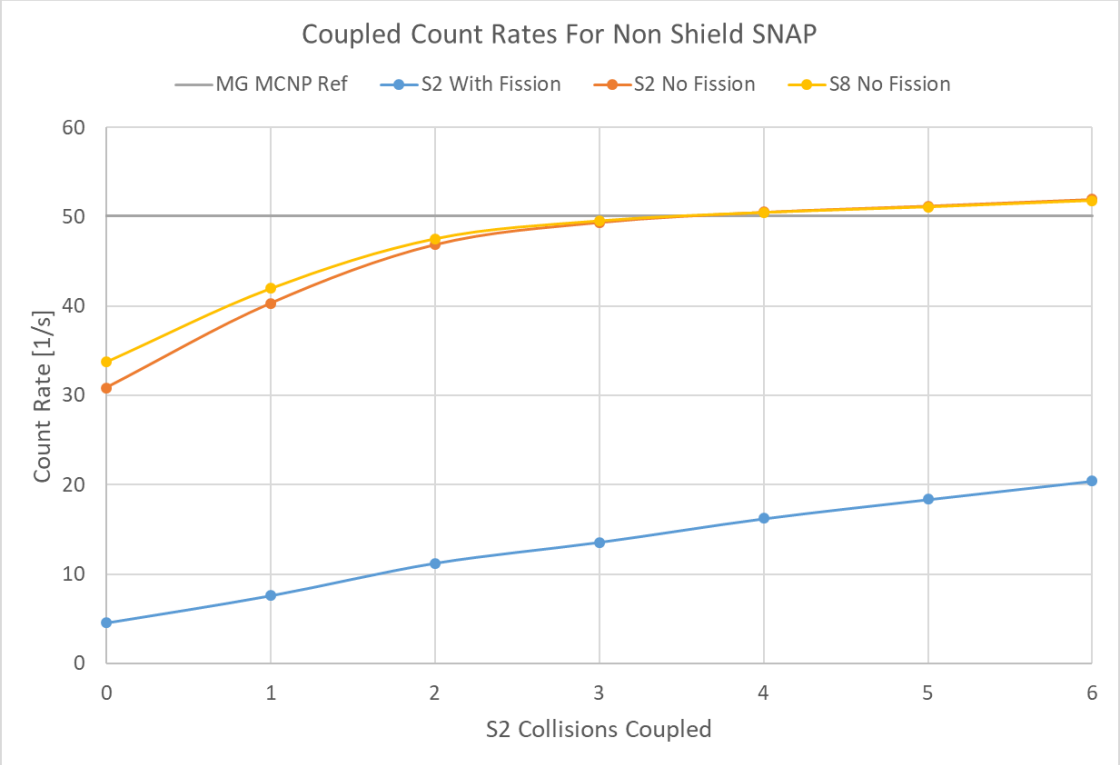

Figure 6.11: Coupled Hammer-THOR Results and Reference Value for SNAP without the HDPE Shield.

It can be observed the calculation with fission appears to be slowly approaching the reference count rates but the calculation without fission is leveling off near the reference count rate value. This demonstrates the effects of a localized source on the method. A more localized

source slows down the mitigation of ray effects through *n*-collided flux and therefore causes the ray effects to persist even at high collision-counts. Alternatively, the secondary source is well distributed in the case with fission turned off. Additionally, the monotonic asymptotic-like approach of the high collision-count results for the coupling without fission adds confidence in the validity of the correction factor applied to the corresponding computations. The fact that the trend of the S_8 calculations is very similar to the trend of the S_2 calculations indicates that even with higher order discrete ordinates calculations, coupling uncollided flux may not be sufficient, and coupling of higher-count flux results from Monte Carlo may be necessary. Indeed, the biggest difference in the S_8 and S_2 seems to be the slightly better count rates for low collided coupling results which are still far from the benchmark result.

The mesh with the HDPE SNAP shield attached was run similarly to the case described above. However, due to the much finer nature of the mesh (see mesh details in Section 5.7.2) the calculation was substantially more expensive than the calculation from the unshielded SNAP version. This system was then only solved with the cheaper fission disabled option for the coupled calculations. Coupled MC-S_N results for this case with fission disabled are shown in Table 6.5.

Table 6.5: Coupled Hammer-THOR Results for the BeRP Ball and SNAP with the HDPE Shield and with Fission Disabled.

N	Collision Order	Count Rate [1/s]	ARE
2	0	11.923	45.84%
2	1	16.976	22.88%
2	2	18.695	15.07%
2	3	19.481	11.50%
2	4	19.644	10.76%
2	5	19.705	10.48%
2	6	19.797	10.07%
16	6	19.771	10.18%

Here the results seem to converge to a common solution very quickly, leveling off after the 2nd or 3rd collided flux is coupled. The S_{16} calculation coupled with the 6th collided flux is almost the exact same value as the 3rd, 4th, 5th, and 6th collided S_2 calculations. This level of agreement indicates that ray effects are almost completely mitigated at these points since the increase in discrete ordinates quadrature order does not substantially alter the computed value.

In a manner similar to the results presented for the case without the HDPE shield, the results in Table 4.1 do not account for errors incurred when meshing the problem, it is then conjectured that the reference value for this problem once meshed is likely closer to the S_{16} calculation coupled with 6th collided flux. Results of coupling solutions from Table 6.5 are plotted in Fig 6.12.

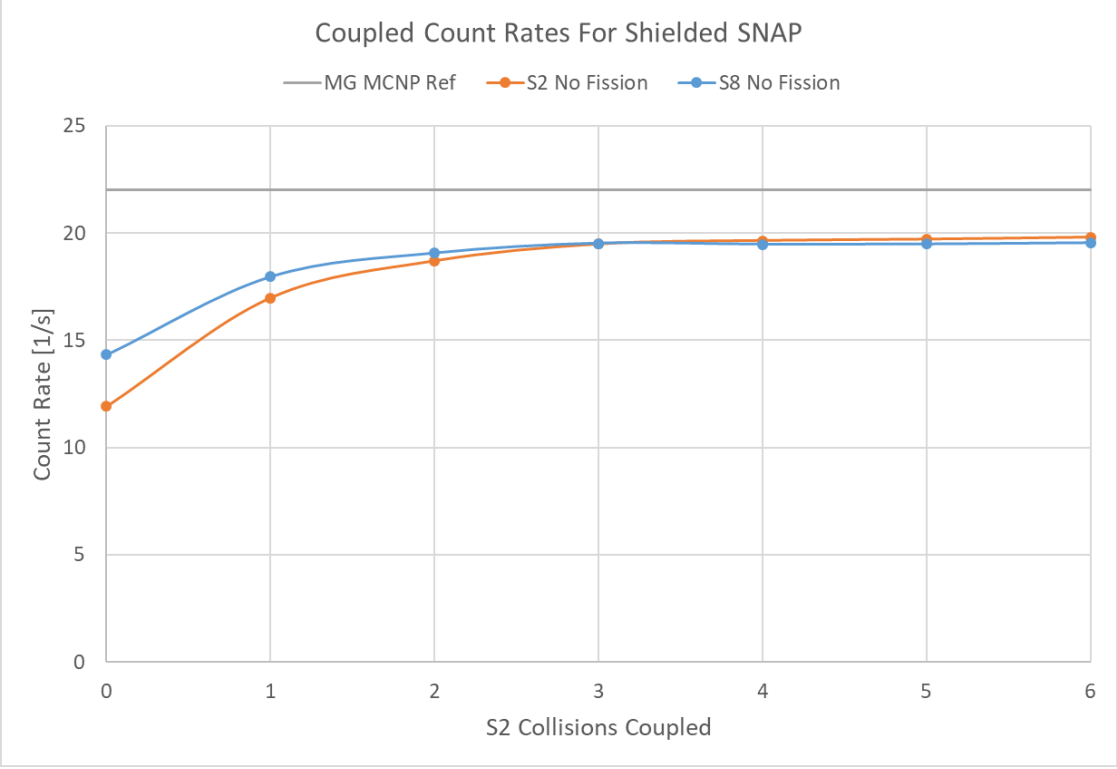

Figure 6.12: Coupled Hammer-THOR Results and Reference Value for SNAP with the HDPE Shield.

It can be observed that the coupled calculation is leveling off in the area of the reference count rates. The manner and rate at which it does so seems to be very similar to the results observed in Fig 6.11. This would indicate that the ray effects have been effectively mitigated. The similarity of the trends in the S_8 coupled calculations to the S_2 indicates that even in more traditional discrete ordinates calculations, higher collision-count coupling may be necessary.

To further illustrate the effectiveness of the method at mitigating ray effects by coupling high collided flux from Monte Carlo simulations, results from coupling 6^{th} collided flux for varying quadrature orders are compared against the same quadrature orders for pure S_N calculations. These results are shown in Fig. 6.13 for both models.

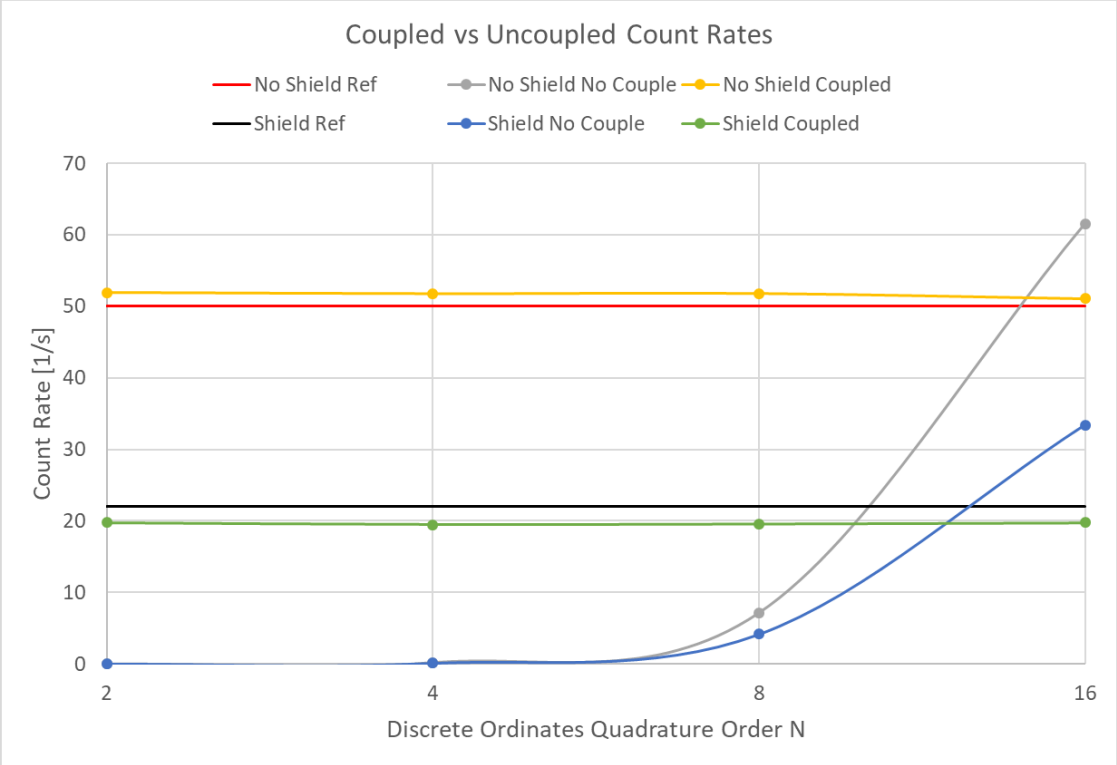

Figure 6.13: Coupled vs Uncoupled SNAP Count Rates with and without HDPE Shield.

These results show that the coupled results are almost completely invariant with respect to quadrature order, indicating that ray effects have been eliminated through coupling of 6^{th} collided flux for this problem. The comparison to the uncoupled results indicates that the

majority of the error incurred in the results was due to ray effects as even the S_{16} calculations are further from the benchmark than any of the coupled results. It also demonstrated the futility of increasing the quadrature order to mitigate the loss of count-rate accuracy in this configuration due to ray effects.

Chapter 7. Conclusions

7.1 Experiments

The experiments described in Chapter 3 show a trend in detector responses based on reflective material around the BeRP ball. The results showed clearly that HDPE reflectors around the ball increased the gross count rate for both the SNAP and MC15 detectors. It also was seen that tungsten and copper reflection had a similar effect as demonstrated in Tables 3.1 and 3.2. This effect is physically due to the increase in neutron multiplication induced in the BeRP ball. As the reflection and moderation from the shells increases, the rate of induced fission increases which in turn increases the total neutrons produced in the plutonium sphere. While the added reflector material also increases the attenuation of neutrons escaping the sphere, this effect is not substantial enough at the thicknesses and materials used in the experiment to overcome the increased multiplications effect on the count rates.

The hypothesis that the addition of the HDPE SNAP shield would have a minimal effect on the count rate of the MC15 was proved in Table 3.2. This indicates that the detectors are almost entirely independent of each other when setup in the manner described in Section 3.1. As such it can be reasoned that a model of the experiment for either detector can be made without inclusion of the other in such a model without incurring substantial errors. The results of the experiments can then serve as independent benchmarks for models created to represent these systems.

7.2 Model and Method Development

Development of the model described in Chapter 4 resulted in a simple configuration that could be meshed into a format compatible with the THOR program as described in Chapter 5.

This model had several errors inherent in it, however the error from each approximated feature has been quantified and a final reference solution was determined for the SNAP model.

To enable the testing of this model in THOR several capabilities and methods were developed and implemented either in THOR itself or as separate auxiliary codes. The subcritical multiplication was successfully implemented and tested against an equivalent method involving an altered scattering cross section. Methods of flux visualization for problem solutions were developed to allow for visual analysis of features of the transport solutions produced by THOR. A successful method of mesh generation and conversion to a THOR compatible format was developed for the widespread CAD modeling software SolidWorks mesh outputs to allow for easier generation of computational models for use in THOR. A utility for converting SERPENT generated cross sections to formats compatible with THOR, MCNP, and Hammer was created to allow for simpler creation of THOR multigroup nuclear data libraries generated by SERPENT. The general collision order MC/S_N coupling method was developed to enable the mitigation of ray effects in THOR calculations. This method was implemented through coupling utilities and finalized by a recombining utility to allow for transparent use of the method even by users unfamiliar with it.

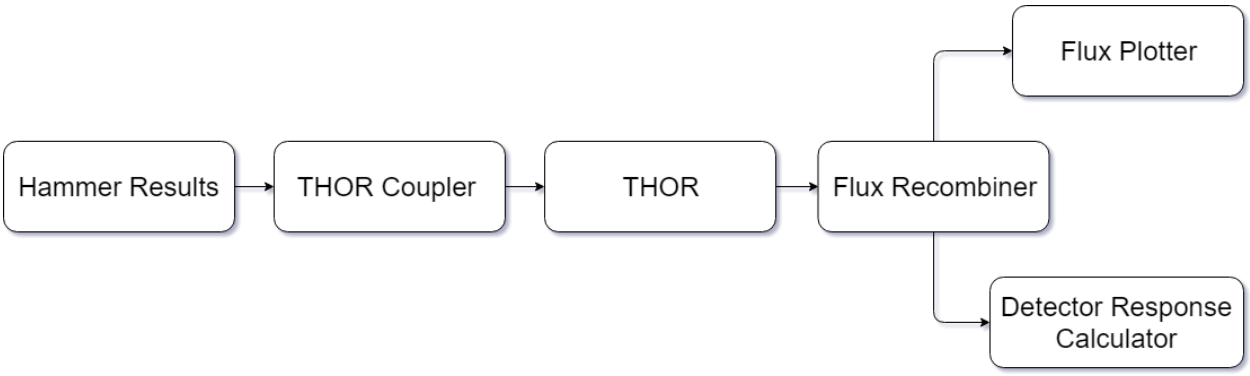

Figure 7.1: Coupling Implementation Flowchart.

Two model configurations were developed to allow for analysis of the effectiveness of the coupling method in two different manners. The first system was composed of just two regions: the BeRP plutonium ball surrounded by a cube of air. This allowed for a system that would suffer severe ray effects far from the localized source in the ball. The relatively low complexity of regions in this configuration allowed for results that could be plotted and easily analyzed for ray effects compared to a reference solution to a similar problem. The second configuration involved the BeRP Ball and the SNAP detector with air separating them for cases with and without the HDPE shield in front of the SNAP. This system was modeled at two different levels of mesh refinement and a utility was developed to allow for THOR results to be integrated in order to create a detector response from the calculation results. Analysis on this model was conducted by comparing SNAP count-rates against MCNP's multigroup simulation results in order to create a more representative reference value of the detector response for this experiment for a given multigroup cross section library.

The model of the plutonium ball in the air box was given the dimensions it has for a reason. The sides of the cube are about the same distance from the BeRP Ball as the SNAP detector is in the actual experiment and the subsequent detector models. This means that visualization of ray effects on the bounding-cube faces of this model are representative of the ray effects that can be expected in the model of the detector system. Similarly, the model was made using air as the ray effect prone material compared to traditional demonstrations of ray effects that involve arbitrarily purely absorbing mediums. This was in order to observe ray effects in the same medium present in the experiment, namely a low-density medium that does not effectively absorb or scatter neutrons.

7.3 Computation Results

The results from the BeRP Ball in the air cube model demonstrated visible ray effects at the mesh outer boundary for all attempted orders of pure discrete ordinates quadratures. Upon application of the coupling to Monte Carlo approach the ray effects had almost completely disappeared from visible observation by the time the S_2 solution was coupled with the 4^{th} collided flux (5^{th} collision source). Even though the S_2 discrete ordinates solutions are prone to the most severe ray effects, due to the small number of constituent angular directions, coupling them with the Monte Carlo collision data resulted in less noticeable ray effects with increasing collision counts than the pure S_{16} calculation. These results demonstrate that in practice ray effects can be substantially reduced by the method proposed in this work.

Pure discrete ordinates calculations performed on the simplified SNAP detector systems (with and without HDPE shield attached) demonstrated that even with the very high order and expensive S_{16} quadrature, obtained results were still far from the reference count rates determined for the same configuration computed with multigroup MCNP simulations. The underestimation of the count rates by the S_2, S_4, and S_8 quadratures is an indication of ray effects causing the source to mostly miss the detector body and then not having an opportunity to propagate into the active helium-3 region. The overestimation by the S_{16} quadrature in both HDPE-shielding cases indicates that the ray effects for these equations are causing the source to be propagated along the rays in a manner so that the active helium-3 region receives more neutrons than it should. This “opposite” ray effect still represents a nonphysical error since the flux along the rays does not experience geometric attenuation As such, it is seen that the best that can be hoped for with ray effects in a detector system is that equal part peaks and troughs of the

rays cancel out the error of the other in such a way as to result in a good computed integral value of the response.

The count rates from the S_2 calculations coupled with Monte Carlo low collision-count flux demonstrates immediate mitigation of ray effects and improvement in the count rate. It can be seen though that the improvement decreases when fission is enabled in the model. This is a result of the secondary source being more localized since fission only occurs in the BeRP ball. However, even with fission enabled the results are still substantially improved for the S_2 calculation which previously yielded an almost zero count rate result. Additionally, the S_{16} count rate is now very much in line with the reference count rate for the multigroup MCNP-computed value. The calculations using the fission correction factors determined via MCNP demonstrate even better ray effect mitigation. For these problems the only secondary source comes from scattering, and scattering happens everywhere in the system not just in the BeRP Ball, e.g. the detector body. This leads to a more distributed secondary source from the Monte Carlo calculation and a better mitigation of ray effects at lower collision-counts. Confidence in the correction factors employed in these calculations is raised as the results line up with the S_{16} coupled results with fission turned on.

The results showing the visual reduction of ray effects suggest that the THOR and the coupling method appear to be functioning correctly due to the similarity to the approximate solution shape. The detector response results and their agreement with the MCNP multigroup solutions provide numerical validation of both THOR and the coupling method described in Section 5.5 in a practical application with a measurable quantity. The presented models can serve as benchmark problems for methods seeking to mitigate ray effects in discrete ordinates calculations, as the selected methods used here are shown to do.

7.4 Numerical Validation of Method for Nonproliferation Applications

The models used had large errors with respect to the experimental results. As such comparison of the coupling method results must be made against the numerical multigroup results from the simplified model in MCNP. A plot demonstrating the gradual progression of the model count rates, hence the incurred error also, and eventual coupling results from THOR and Hammer for the model without the HDPE shield attached to the SNAP detector is shown in Fig. 7.2.

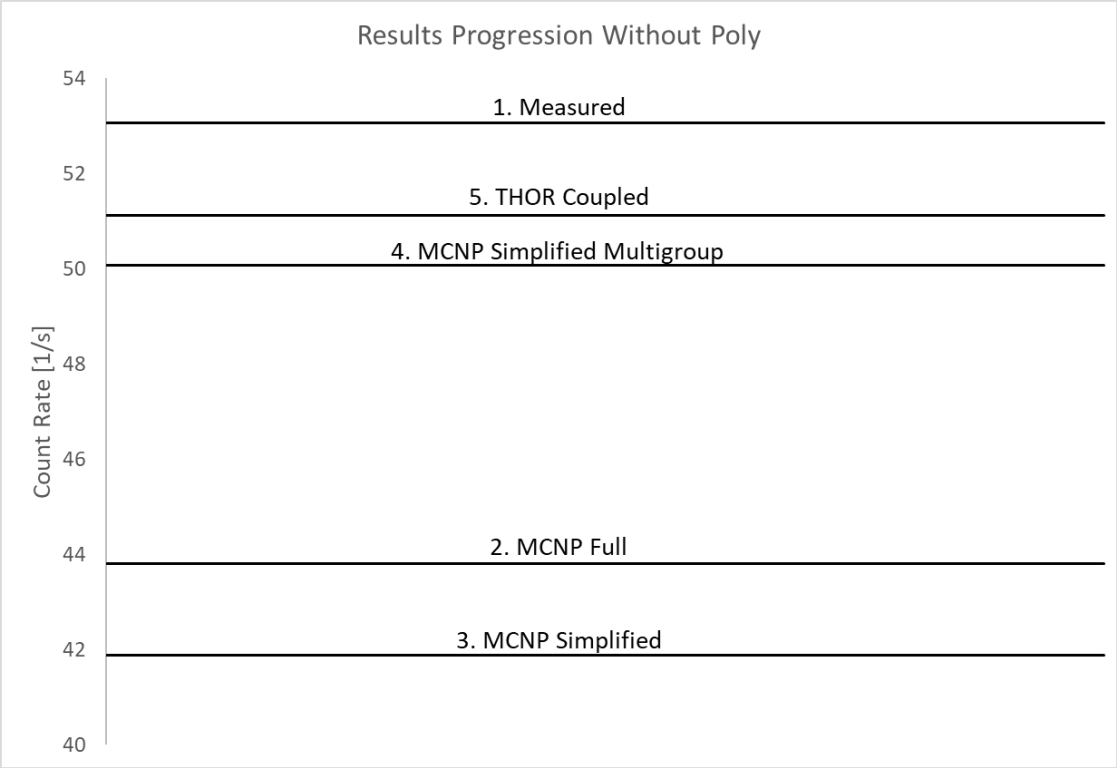

Figure 7.2: Results Progression for the SNAP without the HDPE Shield.

The numbers for each result here represent the progression in the modeling process. The first result is the measured experimental data, this is then followed by the calculation with the full MCNP continuous energy model, which is then simplified to allow for easier meshing. Then a multigroup calculation using the simplified MCNP model and the SERPENT generated

multigroup cross sections (in this case two group with isotropic scattering) is performed and finally compared to the coupled Hammer-THOR results which are also multigroup. Clearly a cancellation of errors happens to cause the final THOR coupled results to be as close as they are to the measured results. This progression is then better illustrated in the case with the HDPE shield attached to the SNAP detector, as in that case the progression is monotonic, so cancellation of errors is less influential on the errors trend. These results are shown in Fig. 7.3.

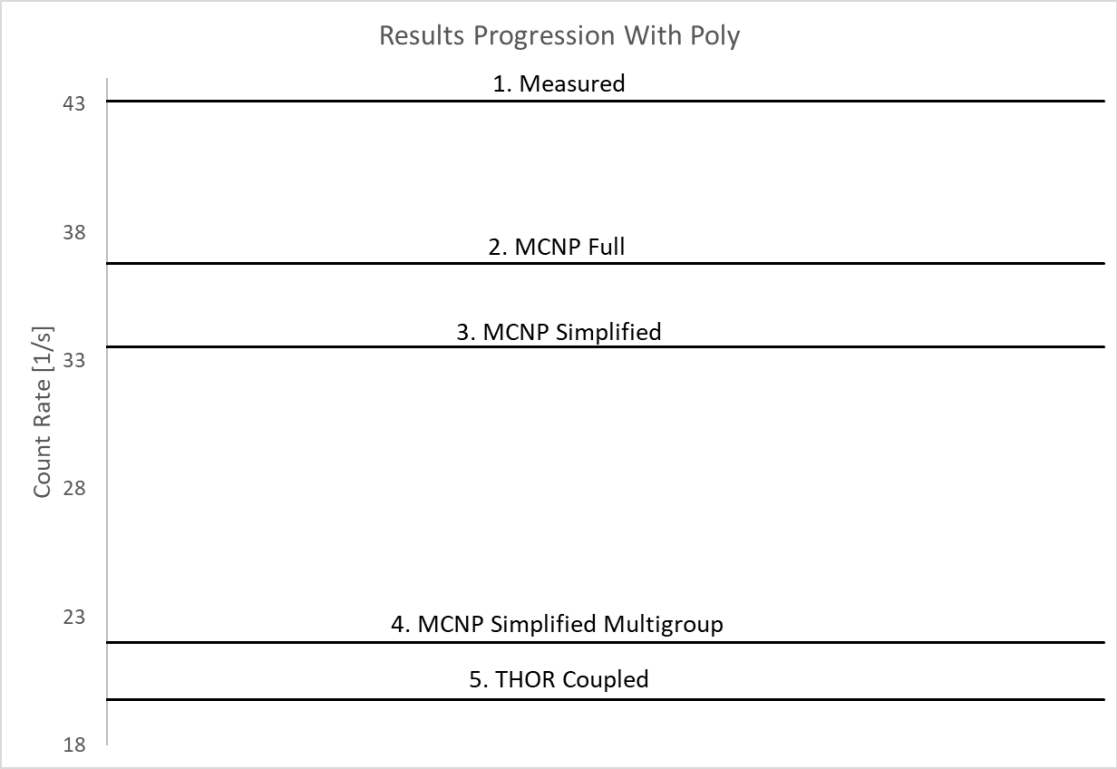

Figure 7.3: Results Progression for the SNAP without the HDPE Shield.

The observation can be made that the largest source of error in both Fig. 7.2 and 7.3 is the multigroup approximation. The cross sections generated for this calculation are only two group and do not feature anisotropic scattering which clearly results in a substantial error in these problems. Due to the large error between the models and the experiment it is impossible to consider these results an experimental validation of THOR and this method. However, the results of the MCNP multigroup calculations represent the configuration being solved in THOR exactly.

The small error between the multigroup MCNP results and the coupled THOR results serves as a numerical validation of the method and THOR for nonproliferation applications.

7.5 Potential Topics of Further Investigation

The coupled Monte Carlo-S_N method has proven to be effective as demonstrated by the work performed and results presented in this Thesis. However, there is still room for improvement in the method application to enhance its effectiveness and generality. Following is a list of preliminary thoughts on areas that can be investigated to improve the application and analysis of the coupling method.

7.5.1 Streamlining the Method's Implementation

The method implementation currently does not require any knowledge of the underlying theory to use since all coupling and analysis are taken care of by external programs with documented and intuitive input parameters. However, the implementation itself is disjointed and requires the sequential running of several different programs. There are reasons that the method is separated in this way, but it could be done in a more streamlined and self-contained manner.

If the CSG model, spontaneous fission source, mesh, and cross sections have already been created, a user running a problem with the coupling method must perform the following steps. First, they must run the problem in Hammer to the collision-count they desire to couple with to obtain the flux for that collision-count from Monte Carlo simulation per Eq 5.7 and 5.8. Next, they must run the coupling utility to produce a useable collision source for THOR to run per Eq 5.10. Then, they must run THOR to get the fully collided flux for the problem per Eq 5.12. This flux needs to the be recombined with the Hammer flux using the flux-combining utility per Eq 5.13. Finally, this total flux can be either plotted by the utilities described in

Section 5.2 or can be analyzed for a region response (active helium in this work) by the response utility.

From start to finish, the implementation requires that the user run a total of five independent applications to calculate the detector response or plot the solution. And this is assuming they have already created a mesh and generated the multigroup cross section library. Since some of these steps take a significant amount of execution time, it also requires the user to return to their work after extended periods of waiting on that step to complete. It would be of use to combine some, if not all, of these applications under a single master program or script that could go from start to finish automatically with a single comprehensive input file (or at least a single input step) so a user could just create the input file(s), run the program, walk away, and return later to examine the full solution. Such a program is certainly possible and would be useful for easier use of the method.

7.5.2 Analysis of Method's Computational Cost

The practical purpose of this method is to capitalize on the lack of ray effects in Monte Carlo methods and the computational speed of discrete ordinates codes. It has been shown in this work that ray effects can be mitigated using the coupling method, however analysis of the speedup associated with the method has not been performed. To this end it would be useful to compare the cost of solving these systems with a full Monte Carlo calculation *versus* the coupled method presented in Section 5.5. Initial analysis could be done with the currently coupled Monte Carlo code Hammer. However, it may be more instructive to analyze the method through coupling with a more established and optimized Monte Carlo code such as MCNP. This would require altering MCNP source code to allow for production of the results required to couple to S_N

in the manner presented here. This analysis would make for a more compelling argument for the practical use of this method in transport problems involving air or other low-scattering media.

7.5.3 Tetrahedral Mesh Runs in MCNP

There is some unquantified error associated in the calculations presented in section 6.2. These results are compared directly to the multigroup MCNP results from section 5.7.1.1 and therefore are compared to a full CSG model. To better quantify the effect that the ray effects and their subsequent mitigation have on the solution of the system, it would be instructive to run a multigroup MCNP simulation on the tetrahedral mesh created for THOR for these systems.

7.5.4 Better Energy Group Representation

Computations for the coupled method described in this work are performed using a two-group discretization of energy. As the number of groups increases, errors in reaction rates should decrease and the accuracy of the solution is expected to improve. As such it is recommended that these problems are also considered for more accurate energy group cross sections with a large number of groups. Splitting up certain material regions may also serve to improve space-energy effects treatment as well. To improve the energy group treatment through increasing the number of groups would only require generation of new cross sections and rerunning the existing models. Splitting material regions may be more complicated though, as it would require remaking certain objects in both SolidWorks for mesh generation and changing the structure of the CSG in SERPENT's input.

7.5.5 Anisotropic Scattering Calculations

While the method presented in Section 5.5 is general and does not impose any requirements on the nature of the problem, the actual implementation is far simpler when considering only isotropic scattering. However, this is a major error introduced in the model.

Now that the method has proven to be effective in achieving its goal of mitigating ray effects, a more robust implementation involving anisotropic scattering would be practical to allow for more accurate neutron transport solutions. Such an implementation would require support of anisotropic scattering on both the S_N and Monte Carlo sides of the problem, as well as angular moments output from the Monte Carlo code.

7.5.6 Experimental Validation

Results in this work provide numerical validation for the ray effect mitigation method and THOR for nonproliferation applications. However, the results of the models are still too far from the experimental results to establish an experimental validation. As such, it is recommended that improvements be made on the models. It is conjectured that the largest improvements to mitigate the most error would be the better treatment of energy groups and anisotropic scattering. This conjecture follows from the fact that the isotropic multigroup cross sections are the largest source of error in the calculation as demonstrated in Fig. 7.1 and 7.2. Additionally, certain restrictions on the model for the sake of computational speed can be relaxed. First and foremost, the lack of the room's floor proved to be a large source of error in Table 4.3. Similarly, the walls and ceiling should be modeled, and other removed or incorrect features can be reincorporated if the meshing capabilities allow it.

Overall though, there is great difficulty in experimental validation. No MCNP model will be able to get the exact correct count rate from the experiments (nor should it, error inherent in the data and experiment description suggests that an exact agreement would be cancelation of such errors). Additionally, tracking error in cross section data from continuous energy Monte Carlo to multigroup discrete ordinates is exceedingly difficult. As such validation will likely take the form of comparisons to continuous and multigroup energy Monte Carlo simulations for high

energy resolution calculations while comparing continuous energy simulations to experimental results.

7.5.7 Multi Direction Coupling

Analysis of these results revealed that when the secondary source was still very localized, the mitigation of ray effects with the method became ineffective. This will be true of any method that mitigates ray effects through a collision source. However, the application of the fission scaling factor hints that there may be practical ways to avoid this restriction. One proposed method involves splitting the solution by collisions after entering a given region rather than collisions after the physical birth of the neutrons. For example, the flux may be solved by discrete ordinates calculations all throughout the BeRP sphere since ray effects are negligible there. The resultant flux exiting the sphere can then be used as input for a Monte Carlo simulation of low collision neutrons and be considered "uncollided" (since they have not experienced a collision after leaving the BeRP Ball yet). Since very few neutrons are reflected back into the sphere from the air, the low-count collided flux calculated by the Monte Carlo code is conjectured to be well distributed throughout the rest of the system allowing for more effective ray effect mitigation.

This method would require more angular communication between the two programs since the scalar flux alone would naturally result in an unrealistically large portion of the exiting flux being sent straight back into the region it is leaving before having a chance to propagate throughout the system.

7.5.8 Application for Reflected BeRP Ball

This work only examined the method as applied to the bare BeRP sphere. However, the experiments examined in Chapter 3 involved different reflectors around the sphere. These

reflectors introduce a large amount of scattering of neutrons born in the sphere before they exit into the air. For this reason, the secondary source in these systems is very localized in the BeRP ball and reflecting shells for low collision-counts. For the direct application of the method to be effective, a potentially prohibitively large number of collisions may be needed to be computed by the Monte Carlo simulation. However, application of the altered method briefly described above in Section 7.5.7 may allow for these types of problems to be computed without the need for very high collision-count coupling. Examination of these experiments would complete the simulation of the experiments described in this work but would likely require a modified method to do so due to the nature of any uncollided or low collided ray effects mitigation method.

7.5.9 Application with MC15

Finally, all of this analysis should also be repeated to simulate the experiment from the perspective of the MC15. The SNAP was chosen for this work since it was determined to be simpler to model and its smaller spatial profile meant that cancelation of errors from ray effects was less likely to occur compared to the much broader faced MC15 detector (since approximately equal cancelling peaks and troughs are less likely to be incident on a smaller face). However, since experimental results and initial MCNP models exist for the MC15, modeling that system and applying the method would serve as further proof of effectiveness. It should be noted though that current limitations mentioned in the method would mean that only one model of the MC15 experiments could be made since the HDPE shield on the SNAP does not affect the MC15 experimental readings.

REFERENCES

[1] S. W. Mosher, R. S. Johnson, A. M. Bevill, A. M. Ibrahim, C. R. Daily, T. M. Evans, J. C. Wagner, J. O. Johnson and R. E. Grove, "ADVANTG—An Automated Variance Reduction Parameter Generator," Oak Ridge National Laboratory, Oak Ridge, TN, 2015.

[2] J. Jung, H. Chijiwa, K. Kobayash and H. Nishihara, "Discrete Ordinate Neutron Transport Equation Equivalent to PL Approximation," *Nuclear Science and Engineering,* vol. 49, no. 1, pp. 1-9, 1972.

[3] R. L. Childs, "GRTUNCL "First Collisison Source Program"," ORNL, Oak Ridge, Tennessee, 1982.

[4] T. M. Evans, A. S. Stafford, R. N. Slaybaugh and K. T. Clarno, "DENOVO: A New Three-Dimensional Parallel Discrete Ordinates Code in SCALE," *Nuclear Technology,* vol. 171, no. 2, pp. 171-200, 2010.

[5] M. M. R. Williams, Mathematical Methods in Particle Transport Theory, London: Butterworth & Co., 1971.

[6] J. J. Duderstadt and L. J. Hamilton, Nuclear Reactor Analysis, Hoboken, NJ: John Wiley & Sons, Inc, 1976.

[7] G. I. Bell and S. Glasstone, Nuclear Reactor Theory, New York: Van Nostrand Reinhold Company, 1970.

[8] I. Lux and L. Koblinger, Monte Carlo Particle Transport Methods: Neutron and Photon Calculations, Boca Raton: CRC Press, 1991.

[9] E. S. Gonzalez, K. A. Beyer, R. J. Fonti, E. C. Leppink, B. D. Rucinski, N. F. Herring, R. Yessayan, S. Schunert, B. C. Kiedrowski and Y. Y. Azmy, "Hammer: A Monte Carlo Particle Transport Solver to Support Nonproliferation Applications of the THOR Deterministic SN Code," in *ANTPC,* Wilmington, 2018.

[10] E. E. Lewis and J. W. F. Miller, Computational Methods of Neutron Transport, La Grange Park: American Nuclear Society, 1993.

[11] R. M. Ferrer and Y. Y. Azmy, "A Robust Arbitrarily High-Order Transport Method of the Characteristic Type for Unstructured Grids," *Nuclear Science and Engineering,* vol. 172, no. 1, pp. 33-51, 2012.

[12] R. M. Ferrer, An Arbitrarily High Order Transport Method of the Characteristic Type for Unstructured Tetrahedral Grids, The Pennsylvania State University, 2010.

[13] K. D. Lathrop, "Ray Effects in Discrete Ordinates Equations," *Nuclear Science and Engineering,* vol. 32, no. 3, pp. 357-369, 1968.

[14] R. E. J. Miller, "The Importance of Discrete-Ordinate Ray Effects in Fast Reactor Design Studies," *Transactions of the American Nuclear Society,* vol. 13, no. 2, pp. 629-630, 1970.

[15] K. D. Lathrop, "Remedies For Ray Effects," *Nuclear Science and Engineering,* vol. 45, no. 3, pp. 255-268, 1971.

[16] W. F. J. Miller and W. H. Reed, "Ray-Effect Mitigation Methods for Two-Dimensional Neutron Transport Theory," *Nuclear Science and Engineering,* vol. 62, no. 3, pp. 391-411, 1977.

[17] M. B. Emmett, W. A. Rhoades, R. L. Childs, J. O. Johnson, W. H. J. Scott and J. A. Stoddard, "A User's Manual for MASH 1.0 - A Monte Carlo Adjoint Shielding Code System," Oak Ridge National Laboratory, Oak Ridge, 1992.

[18] R. A. Lillie, "GRTUNCL3D: A Discontinuous Mesh Three Dimensional First Collision Source Code," in *Proceedings of the 1998 ANS Radiation Protection and Shielding Division Topical Conference,* Nashville, 1998.

[19] F. Masukawa, H. Kadotani, Y. Hoshiai, T. Amano, S. Ishikawa, M. R. Sutton and N. E. Hertel, "GRTUNCL-3D: An Extension of the GRTUNCL Code to Compute R-θ-Z First Collision Source Moments," *Journal of Nuclear Science and Technology,* vol. 37, no. 1, pp. 471-474, 2000.

[20] Y. Y. Azmy, J. O. Johnson, R. A. Lillie, M. J. Rennich and R. T. Santoro, "Computing the Three-Dimensional Distribution of the Gamma Dose Rate in the Target Service Cell of the Spallation Neutron Source Using the DOORS Package," *Progress in Nuclear Energy,* vol. 39, no. 3-4, pp. 321-333, 2001.

[21] I. Prokhorets, S. Prokhorets, M. Khazhmuradov, E. Rudychev and D. Fedorchenko, "Point-Kernel Method for Radiation Fields Simulation," *Problems of Atomic Science and Technology,* vol. 48, no. 5, pp. 106-109, 2007.

[22] R. E. Alcouffe, R. D. O'Dell and F. W. J. Brinkley, "A First-Collision Source Method That Satisfies Discrete Sn Transport Balance," *Nuclear Science and Engineering,* vol. 105, no. 2, pp. 198-203, 1990.

[23] R. E. Alcouffe, "A First Collision Source Method for Coupling Monte Carlo and Discrete Ordinates for Localized Source Problems," *Lecture Notes in Physics,* vol. 240, pp. 352-366, 1985.

[24] J. Mattingly, "Polyethylene-Reflected Plutonium Metal Sphere: Subcritical Neutron and Gamma Measurements," Sandia National Laboratories, Albuquerque, 2009.

[25] R. T. Evans, J. K. Mattingly and D. G. Gacuci, "Sensitivity Analysis and Data Assimilation in a Subcritical Plutonium Metal Benchmark," *Nuclear Science and Engineering,* vol. 176, no. 3, pp. 325-338, 2013.

[26] E. C. Miller, J. K. Mattingly, S. D. Clarke, C. J. Solomon, B. Dennis, A. Meldrum and S. A. Pozzi, "Computational Evaluation of Neutron Multiplicity Measurements of Polyethylene-Reflected Plutonium Metal," *Nuclear Science and Engineering,* vol. 176, no. 2, pp. 167-185, 2014.

[27] D. B. Pelowitz, J. T. Goorley, M. R. James, T. E. Booth, F. B. Brown, J. S. Bull, L. J. Cox, J. W. Durkee, J. S. Elson, M. L. Fensin, R. A. Forster, J. S. Hendricks, H. G. Hughes and R. Johns, "MCNP6 User's Manual," Los Alamos National Security, Los Alamos, 2013.

[28] J. Leppänen, "Serpent – a Continuous-energy Monte Carlo Reactor Physics Burnup Calculation Code," VTT Technical Research Centre of Finland, Espoo, 2015.

[29] J. C. Wagner, E. L. I. Redmond, S. P. Palmtag and J. S. Hendricks, "MCNP: Multigroup/Adjoint Capabilities," Los Alamos National Laboratory, Los Alamos, 1994.

[30] X.-5. M. C. Team, "MCNP — A General Monte Carlo N-Particle Transport Code, Version 5," Los Alamos National Laboratory, Los Alamos, 2003.

[31] KAERI, "http://atom.kaeri.re.kr:8080/ton/index.html," KAERI.

[32] Dassault Systèmes SolidWorks Corporation, "Introducing Solidworks," Dassault Systèmes, 2014.

[33] Autodesk, "AutoCAD," Autodesk.

[34] National Instruments, "NI tutorial on UFF http://www.ni.com/white-paper/4463/en/," National Instruments, 2018.

[35] C. Geuzaine and J.-F. Remacle, "Gmsh Reference Manual," 2017.

[36] B. S. Kirk, J. W. Peterson, R. H. Stogner and G. F. Carey, "A C++ Library for Parallel Adaptive Mesh Refinement/Coarsening Simulations," *Engineering with Computers*, vol. 22, no. 3-4, pp. 237-254, 2006.